ANNUAL REVIEWS

Annual Review of Materials Research

Energy Conversion by Phase Transformation in the Small-Temperature-Difference Regime

Ashley N. Bucsek,[1] William Nunn,[2] Bharat Jalan,[2] and Richard D. James[3]

[1]Department of Mechanical Engineering, University of Michigan, Ann Arbor, Michigan 48109, USA; email: ashley.n.bucsek@gmail.com

[2]Department of Chemical Engineering and Materials Science, University of Minnesota, Minneapolis, Minnesota 55455, USA; email: nunnx029@umn.edu, bjalan@umn.edu

[3]Department of Aerospace Engineering and Mechanics, University of Minnesota, Minneapolis, Minnesota 55455, USA; email: james@umn.edu

Annu. Rev. Mater. Res. 2020. 50:283–318

First published as a Review in Advance on April 21, 2020

The *Annual Review of Materials Research* is online at matsci.annualreviews.org

https://doi.org/10.1146/annurev-matsci-082019-021824

Keywords

energy conversion, small-temperature-difference regime, first-order phase transformation, supercompatibility, ferromagnetism, ferroelectricity

Abstract

The discovery of alternative methods of producing electrical energy that avoid the generation of greenhouse gases and do not contribute to global warming is a compelling problem of our time. Ubiquitous, but often highly distributed, sources of energy on earth exist in the small-temperature-difference regime, 10–250°C. In this review, we discuss a family of methods that can potentially recover this energy based on the use of first-order phase transformations in crystalline materials combined with ferromagnetism or ferroelectricity. The development of this technology will require a better understanding of these phase transformations, especially ferroelectric/ferromagnetic properties, hysteresis, and reversibility, as well as strategies for discovering improved materials.

1. INTRODUCTION TO MULTIFERROIC ENERGY CONVERSION IN THE SMALL-TEMPERATURE-DIFFERENCE REGIME

The discovery of new methods of generating energy without adversely affecting the environment is by any measure one of the most compelling scientific efforts of our time. Climate scientists tell us that, to avoid the predicted 2°C warming, it is not sufficient to make minor improvements in existing fossil-fuel-based energy conversion methods or to replace a fossil fuel with a biofuel (1–5). New zero-emission energy conversion alternatives are needed.

1.1. Waste Heat and the Environment

Due to continuously mounting societal needs, energy is being both consumed and wasted in increasing quantities. In 2008, the International Energy Agency predicted that the growth of global energy consumption would nearly double by 2030 (6); in 2018, it reported that we were already more than 75% there (7). A large proportion of energy consumption is rejected as waste heat, meaning that the available waste heat is increasing with energy consumption. As of 2016, two-thirds of all of the energy produced in the United States was ultimately rejected as waste heat (8). Much of this waste heat comes from industrial sectors, and in some countries, more than 70% of energy consumption is rejected as waste heat (9). In 2008, the US industrial sector consumed one-fifteenth of the power consumed by all sources worldwide, and 25–50% of this power was rejected as waste heat (10). In addition to industry, sources of waste heat include automobiles, power plants, and computers. In particular, the waste heat from computers is a growing problem in light of rapidly expanding systems of clusters containing many thousands of cores. The energy consumption of global data centers accounted for 1.1–1.5% of the total global energy consumption in 2011, equivalent to the average amount of energy consumption in 25,000 American households, and US data centers were responsible for 1.7–2.2% of all US electrical usage; these numbers have been steadily increasing (11–14).

1.2. Energy Stored in the Small-Temperature-Difference Regime

Much of this unrecovered waste heat energy is in the small-temperature-difference regime (10–250°C), where it is difficult to convert heat to electrical or mechanical energy via existing energy conversion technologies (15). **Figure 1** shows some of the sources that contribute to the abundance of energy stored on earth at small temperature differences. An estimated 60% of all industrial waste heat is considered low grade because it exists in this regime (10). Automobiles produce exhaust gases in a temperature range similar to that seen in industrial heat emission, while cooling water in the condensers of power plants emerges at a little less than ~100°C. Microprocessors must also be kept under 100°C to function properly (16). This abundant energy stored at small temperature differences is a growing and drastically underused stockpile of convertible energy.

Besides significant reserves of waste heat from synthetic sources, there are also enormous natural reserves stored at small temperature differences. These include solar thermal sources (17), temperature differences at varying depths in tropical oceans (18), air/water temperature differences in cold climates near large lakes or arctic oceans in winter (19), and temperature differences achieved by radiative sky cooling at 8–13 μm (20). Generally, there is a great variety of environmental sources creating temperature differences of 5–10°C, but these are often fluctuating with variable frequency, mean, and amplitude, which presents a challenge for the design of energy conversion devices.

Recently, the possibility of using first-order phase transformations accompanied by an abrupt change of polarization or magnetization at the transformation has been proposed for energy

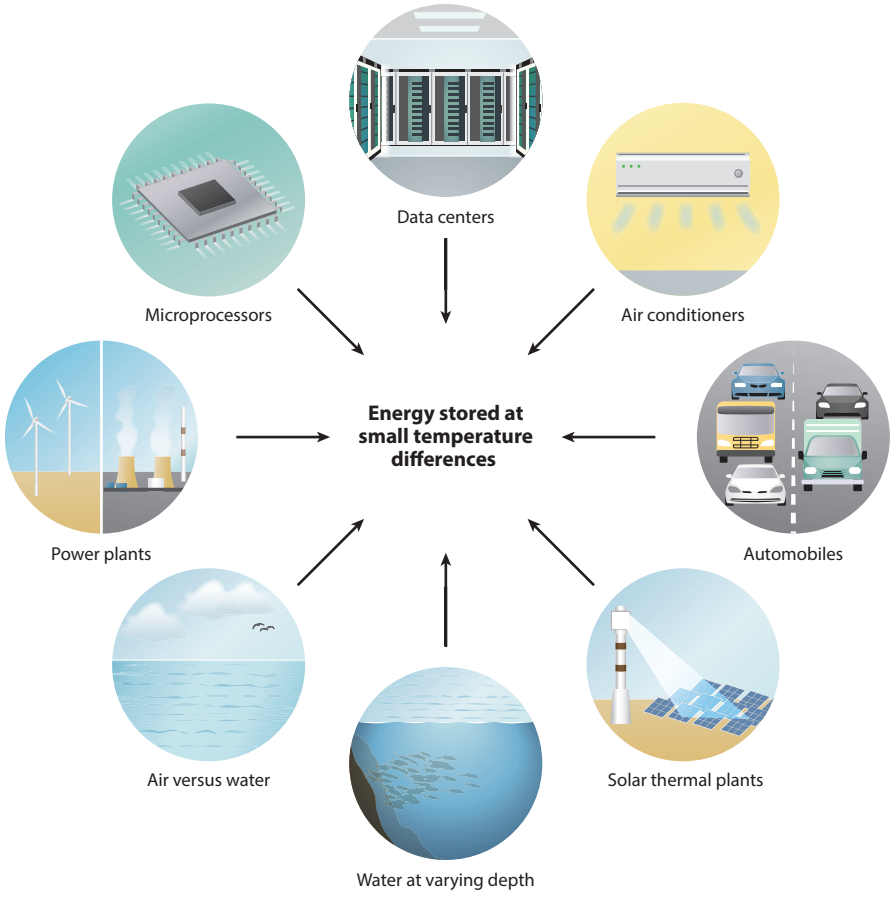

Figure 1

Natural and synthetic sources of energy stored at small temperature differences.

conversion in the small-temperature-difference regime (21–24). We review these methods here. The design of phase-transforming materials that exploit this regime presents a challenge to materials science; it involves materials discovery, identification of suitable phase boundaries, reversibility of the transformation, thermodynamics and design of cycles, and design of devices.

1.3. Alternative Methods

There are a few existing technologies that are applicable to converting energy stored in the small-temperature-difference regime. For the extraction of energy from automobile exhaust gases and computers, and as a source of space power, thermoelectric systems are most often discussed (25). Thermoelectric systems convert temperature gradients to electricity via the Seebeck effect and are applicable to cases where the heat is stored at small temperature differences (26). The performance of thermoelectric devices is measured by a figure of merit, ZT. The most often used thermoelectric material is Bi_2Te_3, which has a ZT of $\sim$1 (27). Thermoelectric materials were a product of the early US space program, with the main thermoelectric properties of Bi_2Te_3 understood as early as 1957 (27). Despite a significant long-term investment, usable materials with a ZT significantly larger than 1 have been slow to emerge.

Among other methods for converting waste heat to electricity, thermogalvanic effects (28), thermo-osmotic vapor transport (29), and the use of liquid crystal elastomers (30) target the small-temperature-difference regime discussed here. Shape memory alloys have first-order phase transformations and can be used as part of energy conversion devices. In that case, a shape memory engine turns an electric generator (31). For this review, we consider only direct energy conversion devices (32), that is, those not having a separate electrical generator.

1.4. Why First-Order Phase Transformations?

There is a sizable body of work on pyroelectric energy conversion methods from as early as the 1960s. The terminology can be confusing. Pyroelectricity is a general term and can be either a single-phase effect or an effect enabled by a phase transformation, and the change in spontaneous polarization can be either small and gradual or large and abrupt.

Pyroelectricity is quantified by an assumption that the spontaneous polarization $P_s(E, \sigma, T)$ is a function of the electric field E, stress σ, and temperature T; the pyroelectric coefficient is then defined (see, e.g., 33) by

$$\frac{\partial P_s}{\partial T}. \qquad 1.$$

The problem with this framework in the context of first-order phase transformations is that $P_s(E, \sigma, T)$ is not an appropriate description of a first-order phase transformation. In particular, a change in the average spontaneous polarization measured upon cooling a material through a first-order ferroelectric phase transformation is due not to an intrinsic change in the polarization of the material but rather to the growth of domains of a new phase that has large spontaneous polarization. Briefly, what is being measured is not a material property but rather the change in the volume fraction of a new phase. In addition, the hypothesis $P_s(E, \sigma, T)$ does not correctly capture standard phase-transformation phenomena such as the effect of stress (and of the stiffness of the loading device) on the transformation temperature; the effect of different ways of applying the electric field (such as the choice of the capacitance of the external circuit) (see Section 5.3); and the effects of hysteresis, microstructure, and—most importantly for energy conversion—the latent heat of transformation. Because we are concerned exclusively with first-order phase transformations in this review, we do not use the term pyroelectricity.

A closely related issue arises in the study of first-order magnetic phase transformations. Early work on the interpretation of magnetic measurements of materials with first-order phase transformations involving an abrupt change of magnetization relied on the assumption $S(M, T)$ for the entropy, where M is magnetization and T is temperature. In single-phase materials, the Maxwell relation,

$$\frac{\partial S}{\partial H} = -\frac{\partial M}{\partial T}, \qquad 2.$$

then provides a way to relate the magnetization and magnetic field measured at different temperatures to the entropy change. For similar reasons as in the ferroelectric case, Equation 2 disagrees with measurements of materials with first-order phase transformations (34). Currently, in the community studying magnetic martensites, there is a better appreciation of the need for accurate models of first-order phase transformations to guide the design of devices, and Equation 2 is used less often.

This distinction between materials with first-order transformations and single-phase materials becomes blurred in the case of partially disordered materials, such as relaxor ferroelectrics (35)

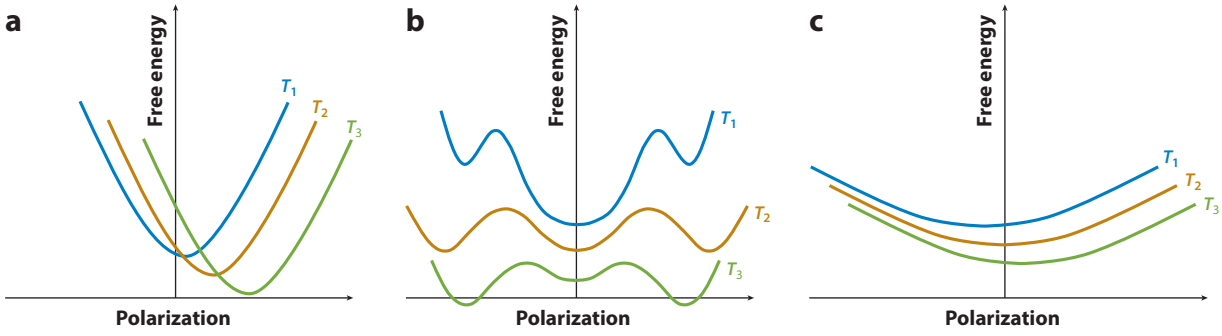

Figure 2

Free energy versus polarization at temperatures $T_1 > T_2 > T_3$ for (*a*) a single-phase pyroelectric material, (*b*) a first-order ferroelectric phase transformation, and (*c*) a relaxor ferroelectric with large disorder.

and glassy ferromagnetic martensites (36, 37). These both have nanoscale inhomogeneity, typically caused by compositional fluctuations or defects. They offer interesting opportunities for energy conversion that circumvent some of the limitations of single-phase materials, and they may give larger accessible temperature ranges than some two-phase materials. Increasingly, critical points are found in materials that undergo first-order solid-solid phase transformations (38–40). Recent evidence suggests that nanoscale inhomogeneity occurs above the critical point, analogous to fluctuations that lead to critical opalescence in fluids. As explained in more detail in Section 5.4, a thermodynamic cycle with both supercritical and mixed-phase parts offers advantages (24) for energy conversion analogous to those of conventional steam generation (41).

Existing work on pyroelectric energy conversion has been performed using relaxor ferroelectrics (42–45) and first-order ferroelectric phase transformations (23, 24), with additional work done either by combining or without distinguishing between ferroelectricity and single-phase pyroelectricity (46–53). Energy conversion using first-order phase transformations in magnetic martensites is undergoing rapid development (21, 22, 54–57) and commercialization (see **http://www.swiss-blue-energy.ch/en/index.html**). Although the study of first-order phase transformations for energy conversion is quite recent, a concept of single-phase energy conversion (near the second-order transition at the Curie temperature) using ferromagnetic materials was patented in 1890 by Tesla (58).

The differences between a single-phase pyroelectric material, a first-order ferroelectric material, and a relaxor ferroelectric material can be seen in their respective free energies, shown in **Figure 2** (59). Fundamentally, the advantage of first-order phase transformations for energy conversion is in the distinct energy wells illustrated in **Figure 2**. The minima of these wells depend on temperature in different ways, giving rise to a large latent heat, according to the Clausius-Clapeyron equation. This large latent heat can be absorbed or emitted during a process at constant temperature simply by changing the volume fraction of the phases. This feature, not available for single-phase materials, is valuable for the construction of high-efficiency cycles such as Carnot cycles. Similarly, there is great flexibility for building adiabats in a two-phase system: Any vertical line in the mixed-phase region of the temperature-entropy diagram is a possible adiabat, and there is additional flexibility to achieve this line, not present in single-phase materials, by again varying the phase fraction together with other variables such as applied fields (**Figure 3**). These advantages are strictly analogous to those of steam generation over single-phase methods such as gas generators.

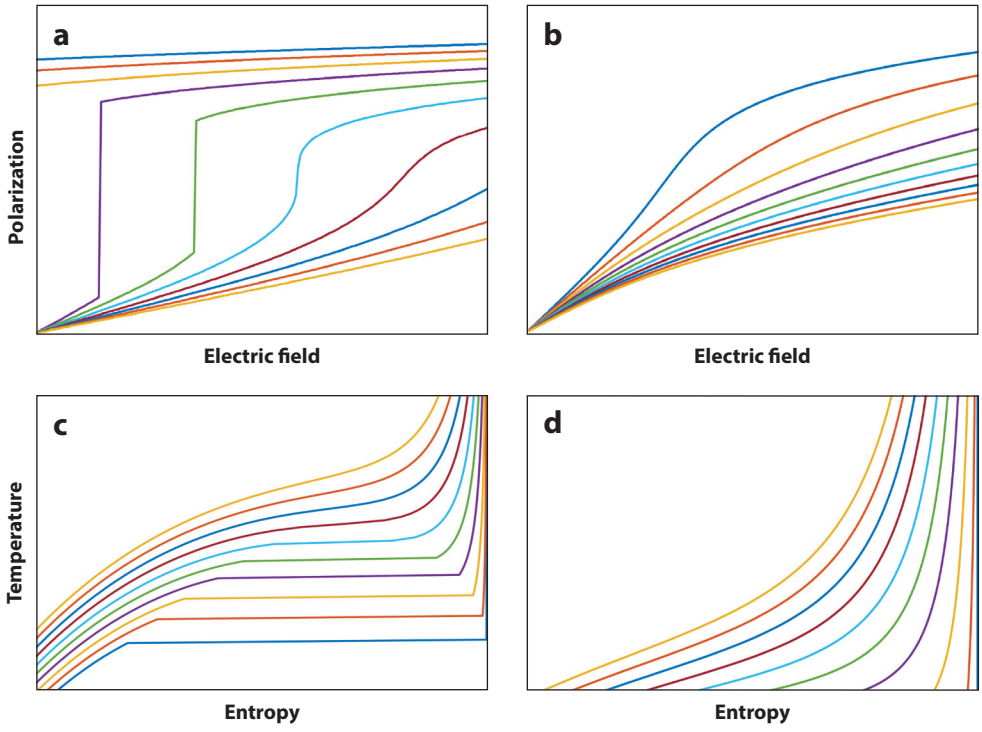

Figure 3

Polarization–electric field diagrams showing lines of constant temperature for (*a*) a ferroelectric material and (*b*) a single-phase pyroelectric material, and temperature-entropy diagrams showing lines of constant electric field for (*c*) a ferroelectric material and (*d*) a single-phase pyroelectric material.

1.5. Plan for This Review

In this review, we focus on technologies that use first-order phase transformations to convert heat to electricity in the small-temperature-difference regime. We cover both ferroelectric and ferromagnetic energy conversion. We strictly limit the scope of this review to materials and devices that use the first-order character of the phase transformation, so, for example, we omit work on most pyroelectric conversion devices, such as those that use relaxor behavior, and ferromagnetic energy conversion near the second-order transformation at the Curie temperature (58). On the other hand, we give evidence that the first-order case holds significant promise.

In Section 2, we introduce some of the materials and discuss why materials that exhibit phase transformations are particularly applicable to energy conversion in the small-temperature-difference regime. In Section 3, we discuss recent advances in phase-transformation research that can be used to engineer low-hysteresis, highly reversible multiferroic materials for cyclic energy conversion devices. In Sections 4 and 5, we discuss energy conversion in the small-temperature-difference regime using ferromagnetic and ferroelectric materials, respectively. In both cases we emphasize the key role of the effect of electric/magnetic fields on transformation temperature, which serves to split the transformation temperatures on heating and cooling and gives rise to a mixed-phase region in the temperature-entropy diagram. We conclude with the ongoing design challenges and opportunities for multiferroic energy conversion research.

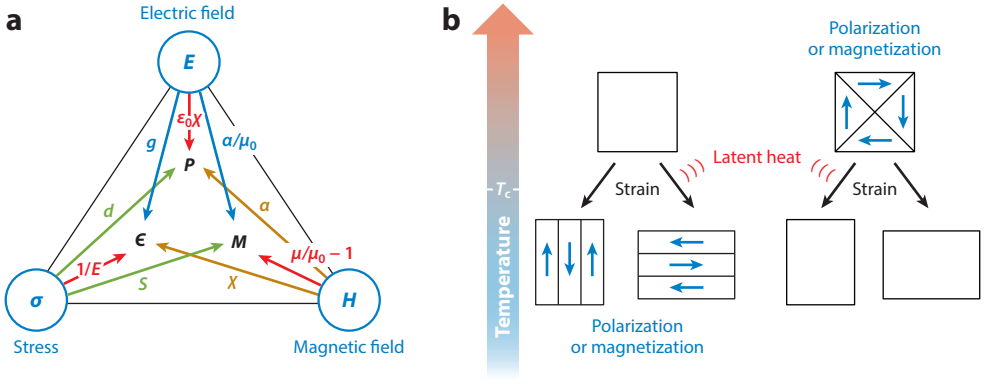

Figure 4

(*a*) Conventional view of multiferroics with linear relations. (*b*) Multiferroism by first-order phase transformation. The temperature axis is vertical.

2. MULTIFERROISM BY FIRST-ORDER PHASE TRANSFORMATION

2.1. Conventional Multiferroics Versus Multiferroism by Phase Transformation

Ferroic materials respond to external stimuli by undergoing spontaneous changes in macroscopic behavior: Ferroelastics, ferroelectrics, and ferromagnetics undergo spontaneous changes in elastic, electrical, and magnetic ordering, respectively. Multiferroic materials exhibit two or all three of these behaviors, where the discrete ferroic behaviors are often coupled. A common conventional view is shown in **Figure 4*a***, with the material constants represented by the labeled arrows—for example, $\sigma = E\varepsilon + dP$. As noted in Section 1.4, the viewpoint in **Figure 4*a*** has little relevance to the present case of phase transformations. A more representative view is shown in **Figure 4*b***. Here, the temperature axis is vertical, the nominal transformation temperature is designated as T_c, and often very large transformation strains are accompanied by an abrupt change of polarization or magnetization. Either the high- or the low-temperature phase (or both) can exhibit strong magnetization or polarization. Critical to energy conversion applications, an often large latent heat is released or absorbed during the phase transformation.

Among currently known materials in which large strain, magnetization, and polarization coexist, many more fall into the scheme of **Figure 4*b*** than into that of **Figure 4*a*** (60–62). This is because polarization and magnetization are sensitive to lattice parameters, and large changes are therefore possible at a phase transformation.

When applied to phase transformations, even the basic idea that, for example, strain and polarization cause stress is incorrect. Rather, the free energy of the material depends in general on the fields of strain, polarization, magnetization, and temperature, and free energy minimization (or local minimization) leads to relations among these quantities. Depending on the situation, applied fields and loading devices contribute additively to the free energy and bring in other quantities like stress and fields. An explicit example from energy conversion that illustrates the absence of the cause-and-effect relation of conventional multiferroics is presented in Section 2.5.

There are significant similarities between phase transformations in crystalline metals and in oxides, but the terminology tends to obscure these. As noted above, we avoid the term pyroelectricity because it is imprecise. The term martensitic phase transformations, originally applied to steels (e.g., 63), has become popular for first-order diffusionless phase transformations in general (32, 64–70) and in particular for metallic alloys that have an abrupt change in magnetization. Of course, for high-power energy conversion, diffusion is unwanted.

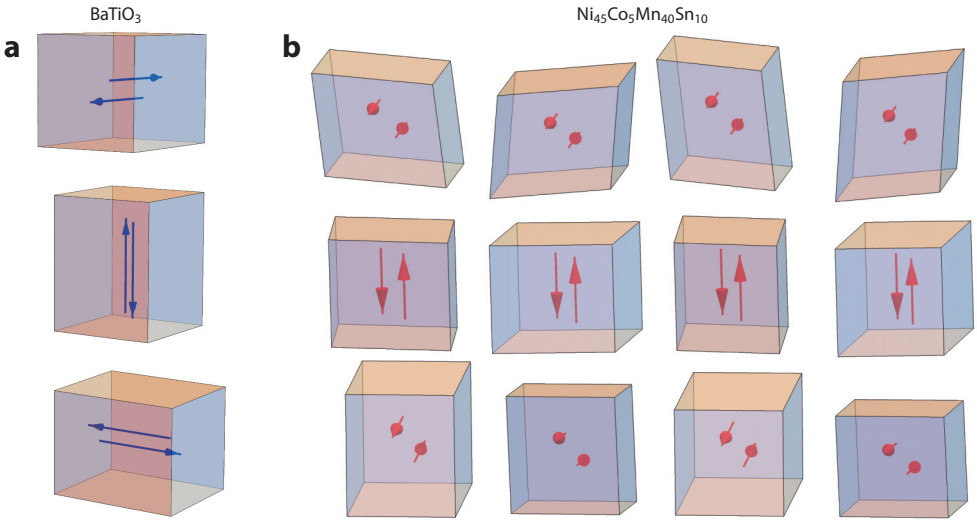

Figure 5

(*a*) Variants of $BaTiO_3$ with easy axes of polarization (*blue*). (*b*) Variants of $Ni_{45}Co_5Mn_{40}Sn_{10}$. The red arrows show typical magnetizations for a magnetic martensite with a twofold monoclinic easy axis. To make the distortions easily visible, the strains are multiplied by a factor of 50 for $BaTiO_3$ and 5 for $Ni_{45}Co_5Mn_{40}Sn_{10}$.

During phase transformations, the material typically transforms from high-symmetry to low-symmetry crystallographic phases. $BaTiO_3$ undergoes three ferroelectric transformations on cooling: cubic to tetragonal to orthorhombic to trigonal. The cubic phase is paraelectric, and the other phases are ferroelectric. In ferromagnetic $Ni_{45}Co_5Mn_{40}Sn_{10}$, a strongly ferromagnetic high-temperature cubic austenite phase transforms on cooling to a nonferromagnetic, monoclinic martensite phase. These two prototypical examples are used in Sections 2–5 to illustrate energy conversion concepts, but many other choices are possible among modern functional materials. Among crystalline materials with first-order phase transformations, energy conversion devices using $(MnFe)_2(P,As)$ (54), $Ni_{50.4}Co_{3.7}Mn_{32.8}In_{13.1}$ (55), $Ni_{51.4}Mn_{28.3}Ga_{20.3}$ (56), and La-Fe-Co-Si (57) have also been demonstrated.

2.2. Crystallography of the Transformation

Due to the symmetry disparity between phases, there can be several different distortions of the parent phase that produce the low-temperature phase. These martensite orientations are called correspondence variants—or, simply, variants—and the number of variants is equal to the number of orthogonal transformations in the parent point group divided by the number of orthogonal transformations in the martensite point group (69). Often, invariance of the free energy density under $\pm\mathbf{M}$, where $\mathbf{M}$ is the magnetization, is assumed independently. In our canonical examples, $BaTiO_3$ has six variants (corresponding to three strains), while $Ni_{45}Co_5Mn_{40}Sn_{10}$ has 24 variants (corresponding to 12 strains) (see **Figure 5**).

2.3. Models for Multiferroic Phase Transformation

At all levels, the development of models of multiferroic phase transformations presents major challenges. First principles methods have been valuable for locating new phase boundaries or, often,

for defining more precisely the physics of the transformation once such a boundary is indicated experimentally. Among these methods, those for ferroelectrics are developed to the highest level (71). The further development of these methods in the context of energy conversion is challenging, because it confronts some of the fundamental bottlenecks of density functional theory: positive temperature, nonstoichiometry, strong correlation, and microstructure.

Continuum theories are equally challenging. Typically, one has to deal with finite deformations to account for the big crystallographic changes, and magnetization and polarization live on the deformed/transformed configuration (72, 73). Furthermore, the stray fields produced by magnetization and polarization live on all of space, and their demagnetization/depolarization effects are important in the cases of greatest interest—that is, when the saturation magnetization or polarization is large. In particular, the shape effect (62) is very significant, as explained in Sections 4.2 and 4.3.

The devices have external circuits, capacitors, permanent magnets, or coils, so the above models of free energy have to be linked with the electrodynamics of induction and capacitance in the external circuit. The inherent quasi-static assumption of instantaneous energy minimization may fail at high rates, implying the need for a fully dynamic model.

Modeling is an essential component in the development of multiferroic energy conversion. In fact, the simple models presented throughout the article have been remarkably useful, and surprisingly, they give reasonable quantitative answers (22–24, 74). A simple example is the free energy, $\varphi(M, T)$, as a function of average magnetization M and temperature T. For the modeling of φ, one can use reasoning analogous to the way density functional theory is related to full quantum mechanics—that is, partial minimization (75). Specifically, one can fix the volume-averaged magnetization and temperature and conceptually minimize all the other variables in one of the general models (72, 73), as described in the appendix of Reference 76. Then these models predict that derivatives of $\varphi(M, T)$ are related to measurable quantities: $-\partial\varphi(M, T)/\partial T$ to calorimetry via the usual relation between entropy and heat absorbed, and $\partial\varphi(M, T)/\partial M$ to magnetization versus applied magnetic field measurements of the given specimen. The only caveat is that because of the shape effect arising from the demagnetization energy, if one merely changes the shape of the specimen, then one has to remeasure magnetization versus magnetic field or else correct the original data by the careful use of demagnetization matrices.

2.4. Domain Engineering

There are likely to be significant breakthroughs in the efficiency and power output of energy conversion devices as a result of domain engineering. Here, we lump under the term domain engineering the manipulation both of twin boundaries between variants, which may or may not coincide with domain walls, and of domain walls within a variant. Domain engineering relating to the reversibility of the phase transformation is discussed in Section 3.

One of the simplest results on domain structure underlies the prospects for energy conversion in these materials. As mentioned in Section 2.1 (see also **Figure 5**), we often have variants of the ferrophase, related by the point group relationships. In fact, in materials with a cubic parent phase, variants are often related by a twofold operation—that is, reflection or 180° rotation—since there are lots of these operations in any of the cubic groups. A classic result is that a pair of variants related in this way can always be twinned, and the twinning is of type I or II (69). In this case, one has the following theorem (73, 77):

$$\text{mechanical compatibility} + \text{reflection (or } 180^\circ\text{) symmetry} \Longrightarrow \text{no poles.}$$

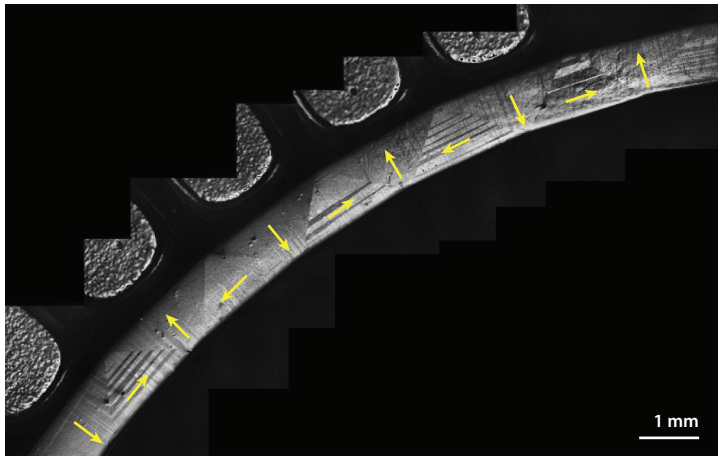

Figure 6

A pair of alternating twin variants with magnetization (*yellow*; added by hand) in $Ni_{50}Mn_{28}Ga_{22}$. The round posts are permanent magnets with alternating polarity. The magnetization is exactly pole-free on the internal twin/domain boundaries. The occasional stripes within the triangles are modulation twins, explained in References 144 and 145. Figure adapted with permission from Reference 146.

This is illustrated in **Figure 6**, where one can see that the interior boundaries of the triangles are perfectly pole-free. It can also be appreciated geometrically: If there is mechanical compatibility, then the variants fit together, and the crystal lattices across the boundary are related by reflection or 180° rotation **Q**. If this operation is applied to, say, the easy-axis magnetization $\mathbf{M}_1$, and one also makes a suitable choice of ± 1, then the resulting magnetization $\mathbf{M}_2 = \pm \mathbf{Q}\mathbf{M}_1$ is crystallographically equivalent to the original one for the second variant, and it automatically satisfies $(\mathbf{M}_2 - \mathbf{M}_1) \cdot \mathbf{n} = 0$, where $\mathbf{n}$ is the normal to the twin boundary. The generic ability to have exactly pole-free interfaces with magnetization/polarization on easy axes in highly deformed, complex arrangements of type I/II (or compound) twins permits low-energy rearrangement of the phases.

Domain engineering is expected to be particularly useful in thin-film-based devices where epitaxial strain can also be used to modify transformation temperature and constrain microstructure. Recent advances in thin film growth techniques now allow the fine control of material composition, strain, microstructure, and defects, which in turn facilitates materials design with engineered domain structure. Additionally, these features allow precise control of composition that can be used to satisfy conditions of supercompatibility (Section 3). Among these approaches, hybrid molecular beam epitaxy (MBE) is particularly promising in the ferroelectric case, in that it yields epitaxial perovskite films with exceptional structural and electronic quality (78–81). In general, the hybrid MBE approach combines the advantages of chemical vapor deposition and conventional MBE approaches. Through the co-deposition of metal organic and solid elemental precursors, hybrid MBE allows for precise control over material stoichiometry, which plays an important role in ferroelectric and ferromagnetic properties. Taking advantage of epitaxial strain, one can modify crystal lattices via growth on a variety of commercially available substrates. Microstructure can be manipulated through the choice of mechanical and electrical boundary conditions provided by the underlying substrate (81). The method gives unprecedented control over defect types and densities (82). These multiple levels of control allow for precise tuning of desirable multiferroic characteristics such as phase transition, reversibility, transition temperatures, and the strength of polarization or magnetization.

2.5. Critical Role of the Effect of Field on Transformation Temperature (the Clausius-Clapeyron Relation)

The single most important factor to consider when designing an energy conversion device based on a first-order ferromagnetic or ferroelectric phase transformation is the effect of the electric field (in the ferroelectric case) or the magnetic field (in the ferromagnetic case) on transformation temperature. It is that effect, produced by external coils or capacitors, that splits the transformation temperature on heating from that on cooling and opens up the mixed-phase region shown in **Figure 3**.

It is not sufficient to heat and cool a specimen through a ferromagnetic or ferroelectric phase transformation at temperature T_c. Such a process will produce a horizontal line at $T = T_c$ in the temperature versus entropy diagram and will give no electrical work. More precisely, in such cases, the exact amount of electrical work produced on polarizing the material by cooling through the phase transformation at T_c will need to be supplied by the external circuit to depolarize the material on the reverse transformation at T_c.

The work produced by the cycle is equal to the area inside the closed process loop, and the efficiency is the ratio of the area inside the loop to the sum of the areas inside and below the loop. It is therefore advantageous to have a large mixed-phase region to enable high-efficiency, high-work-output Carnot and Rankine cycles. In a ferroelectric/ferromagnetic energy conversion cycle, a part of the cycle takes place at higher electric/magnetic fields, and a part of the cycle will take place at lower electric/magnetic fields. More specifically, forward transformation will occur at higher electric/magnetic fields, and reverse transformation will occur at lower electric/magnetic fields, or vice versa. To obtain particular cycles, it is necessary to vary the transformation temperature in a particular way through the use of time-changing applied fields, designed using the Clausius-Clapeyron equation.

The classical example of the Clausius-Clapeyron relation is that of water boiling under pressure—that is, boiling point elevation or depression. The Clausius-Clapeyron relation governing this effect is

$$\ln\frac{P_2}{P_1} = -\frac{L}{R}\left(\frac{1}{T_{c,2}} - \frac{1}{T_{c,1}}\right), \qquad 3.$$

where R is the specific gas constant, L is the latent heat of transformation, and $T_{c,1}$ and $T_{c,2}$ are the transformation temperatures at pressures P_1 and P_2, respectively.

First-order phase transformations in ferroelectrics and ferromagnetics are directly analogous to the first-order phase transformations in water/steam, and the Clausius-Clapeyron relation can be used to describe the effect of stress or fields on ferroelectric and ferromagnetic transformation temperatures. As an example, we take a simple model, $\varphi(P, T)$, of the free energy per unit volume of the ferroelectric case as a function of polarization P and temperature T, which has energy wells corresponding to paraelectric and ferroelectric phases. The quantity $A_f d_f \varphi(P, T)$ is the free energy of a ferroelectric plate of thickness d_f and area A_f. In a simple system of interest, depicted in **Figure 7**, this ferroelectric capacitor is joined in parallel to an ordinary capacitor. Since free charges are allowed to flow to the electrodes (assumed ideal) of the ferroelectric capacitor and internal interfaces are expected to be pole-free (cf. **Figure 6**), we omit depolarization energy. The circuit is charged by a battery. After the battery is detached, the closed system, in the sense of Gibbs, consists of the ferroelectric and ordinary capacitors with total free energy $A_f d_f \varphi(P, T) + \frac{1}{2} C_o V^2$, where C_o is the capacitance of the ordinary capacitor. Therefore, the appropriate minimization

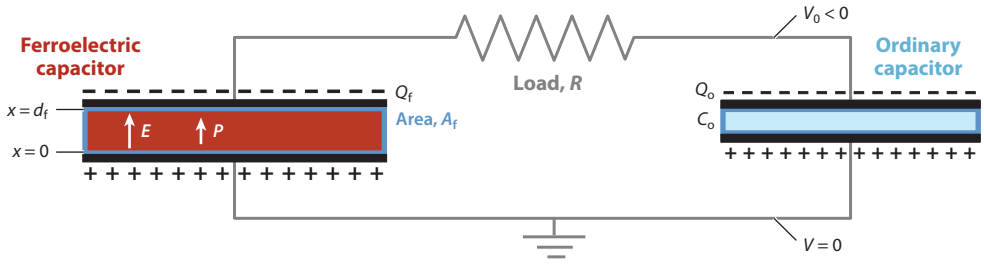

Figure 7

Schematic of the simplest energy conversion device using a ferroelectric phase transformation (24). The phase-change material is shown in dark red.

problem is

$$\min_P \left[A_f d_f \varphi(P,T) + \frac{1}{2} C_o V^2 \right], \tag{4.}$$

given $Q_{tot} = Q_o + Q_f = C_o V - A_f P$. The given quantity is the total charge Q_{tot}, which distributes itself between the two capacitors according to energy minimization. The minimization of Equation 4 over P with Q_{tot} given is not the same (24) as the often quoted minimization problem

$$\min_P \left[A_f d_f \varphi(P,T) - EP \right], \tag{5.}$$

given E. However, the first variation of Equation 4 gives the condition

$$\frac{\partial \varphi(P,T)}{\partial P} = -\frac{V}{d_f} = E, \tag{6.}$$

which is the same as the condition given by the first variation of Equation 5.

The Clausius-Clapeyron equations based on Equations 4 and 5 are different. These are obtained in both cases (and in the case of water/steam) by allowing T to vary and seeking conditions under which there are two absolute minimizers, $P_p(T)$ and $P_f(T)$, corresponding to paraelectric and ferroelectric phases, respectively; asserting that total energies at $P_p(T)$ and $P_f(T)$ are the same; and differentiating with respect to T (see 24). In the case of Equation 5, the result is

$$T'(E) = T_c \frac{P_f(T) - P_p(T)}{L}. \tag{7.}$$

The minimization problem in Equation 4 gives a different Clausius-Clapeyron equation. These two become the same when the following holds:

$$\frac{A_f P_f^2}{2(\Delta \mathcal{E}) d_f C_o} \ll 1, \tag{8.}$$

where $\Delta \mathcal{E}$ is the maximum difference in free energy density occurring during a cycle. In general, on the uncharted ground of energy conversion, it is wise when selecting the closed system to consider possible free energy contributions of the external circuit, field-producing sources, or loading devices, rather than to blindly use Gibbs functions that are designed for idealized sources (see 24, appendix).

3. SUPERCOMPATIBILITY, SUPERCRITICAL BEHAVIOR, AND THE REVERSIBILITY OF PHASE TRANSFORMATIONS

3.1. Requirements for Energy Conversion in the Small-Temperature-Difference Regime

The basic requirements for a general energy conversion technology are noted in Section 1.4: large electrical work output per cycle, high thermodynamic efficiency, and high power density. For an energy conversion device that operates via cycling, the processes must also be stable for millions of cycles. For example, operation at 1 Hz for 10 years gives about 315 million cycles. Thus, the multiferroic must have a highly reversible phase transformation and low hysteresis, which is the main source of loss in existing devices. These two factors—hysteresis and reversibility—are believed to be related, but each also has influences that do not affect the other.

Our terminology is the following: Reversibility refers to a cyclic process in which the device returns to its original state at some time during the process. Thus, a process with hysteresis, which cannot be completely eliminated in first-order phase transformations, can still be reversible. For example, a suitably fabricated alloy $Ti_{54.7}Ni_{30.7}Cu_{12.3}Co_{2.3}$ (83) returns to its original state at zero strain within experimental error after 10 million cycles of stress-induced full transformation, but each cycle has quite large hysteresis.

On the side of materials design, two recent developments in the study of phase transformations—supercompatibility and supercritical behavior—have particular importance for energy conversion.

3.1.1. Hysteresis. There are two accepted views of the origins of hysteresis in phase transformations, one intimately connected with the reversibility of the transformation (84) and the other unrelated to reversibility (85). Experimental observations suggest that one or both can be operative, depending on the material and conditions (86).

The first view is related to structural fatigue. Measurement of the migration (87, figure 1) or shape changes (83, figure 1*a*) of the hysteresis loop during cycling is believed to be related to structural changes in the crystal, such as the formation of dislocations and other defects (88, 89). The understanding of hysteresis relating to structural fatigue begins with the typical transformation mechanism of a nominally reversible first-order phase transformation, whether in a ferroelectric, ferromagnetic, or martensitic crystal. This is via the movement of austenite-martensite interfaces.[1] In phase transformations, it is well known that, in most materials, there is no plane, or interface, where the austenite and martensite phases can meet while maintaining perfect compatibility. Yet in the mixed-phase region (as shown in **Figure 3*a*,*c***), both phases coexist. To do so, the martensite phase forms fine mixtures consisting of alternating laminates of twinned martensite variants extending away from the austenite-martensite interface (see **Figures 8** and **9**), with the elastic energy confined to a layer near the interface, which is schematized in **Figure 8**. As shown in **Figure 8*b–d***, this elastic transition layer can be reduced while keeping the strains exactly the same, but at the expense of increasing the interfacial energy on the twin boundaries. The observed configuration is the winner via energy minimization of the competition between elastic energy in the transition layer and interfacial energy on the twin bands.

[1]We use the terminology from martensitic phase transformations here, since the understanding of these interfaces came from the study of martensites (64, 65, 90–92). Austenite-martensite interfaces (**Figure 8**) are very often observed in the wider class of phase transformations, with additional order parameters relating to ferroelectricity or ferromagnetism. In our opinion, this is likely due to the fact that interfaces present in nonmagnetic, nonpolar martensites remain pole-free when polarization or magnetization is present (Section 2.4).

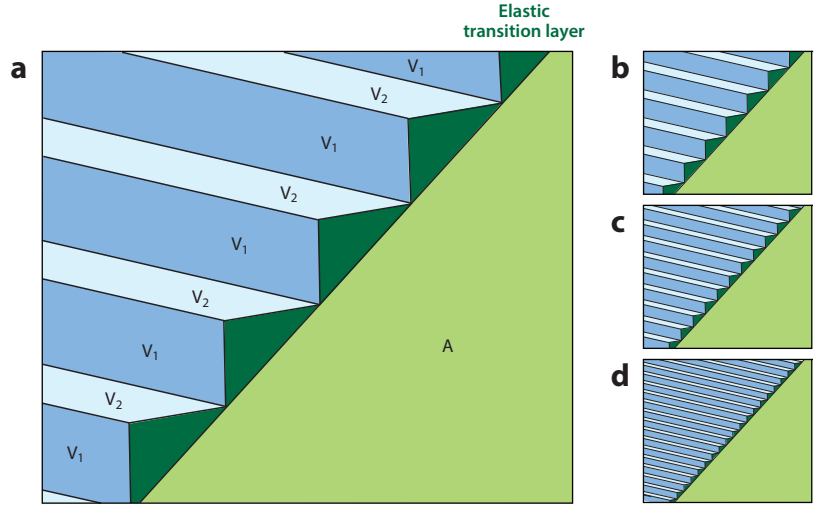

Figure 8

(*a*) Schematic of an interface between austenite and a fine mixture of martensite twins; V_1 is martensite variant 1, V_2 is martensite variant 2, and A is austenite. (*b–d*) As the martensite twins get finer and finer, the elastic transition layer decreases.

An alternative kind of transition layer between austenite and martensite is often seen in both nonmagnetic and magnetic martensites (93, 94). This consists of branching of the twins, which saves interfacial energy away from the austenite-martensite interface, where refinement is not needed. The penalty for this is a slight rotation of the twin boundaries, which has the effect of delocalizing the elastic energy (95, 96).

For both types of interface, there is a stressed interfacial layer. During transformation, each point in the material sees this interface at least once (typically once, if there is no retransformation).

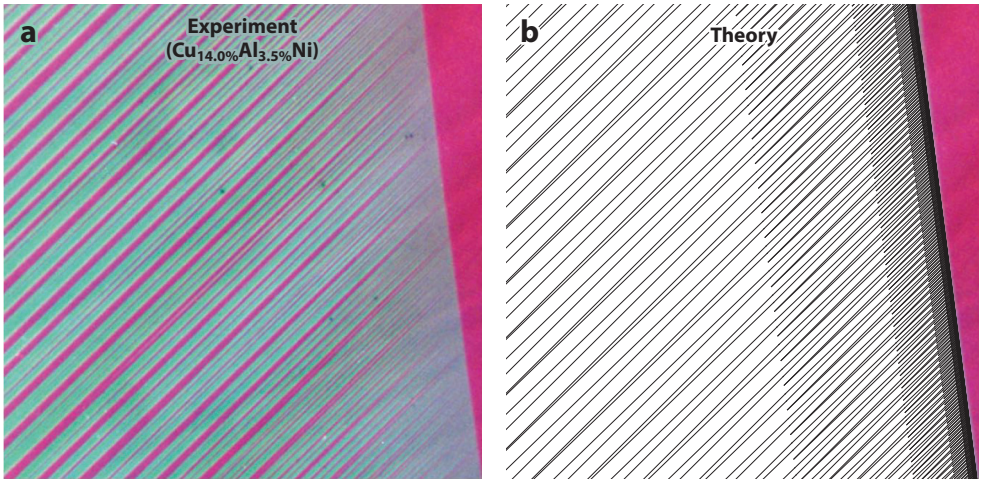

Figure 9

(*a*) A branched austenite-martensite interface in $Cu_{14.0\%}Al_{3.5\%}Ni$ (mass percent). (*b*) A theoretical model of this interface (96) evaluated for this alloy, which exhibits a lower energy scaling than that shown in **Figure 8**. The pink triangle on the right is austenite in both panels.

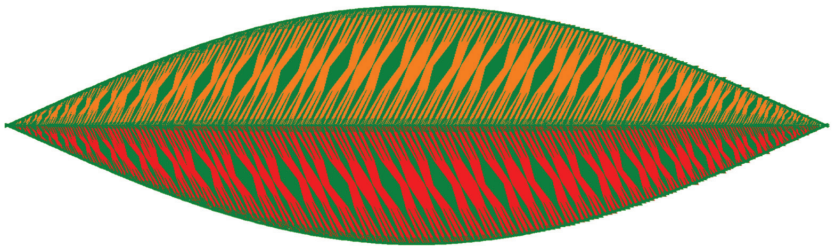

Figure 10

Sketch of a twinned platelet from the theoretical model of nucleation presented in Reference 147. In this case, the internal bands are branched twins. Figure reprinted from Reference 147 with permission from John Wiley and Sons.

The first idea of hysteresis theorizes that the passage of this stressed layer causes damage in the material, leading to effects like migration or distortion of the hysteresis loop. In addition, the energy dissipated as heat during the formation of defects may contribute to hysteresis.

A second idea for the origins of hysteresis does not necessarily imply damage to the material and therefore is compatible with cyclic reversibility. This idea concerns a particular energy barrier that is believed to relate to nucleation of a platelet, schematically shown in **Figure 10**. Numerous observations (85) point to nuclei of austenite already present at low temperatures and, similarly, nuclei of martensite present at high temperatures. Micrographs of martensite nuclei in austenite, for example, suggest the relevant nucleus is a twinned platelet bounded by two austenite-martensite interfaces and stabilized by a defect (e.g., a triple junction). Beginning in austenite, the platelet is expected to grow upon cooling because of the bulk energy difference between austenite and martensite. However, the subtle interplay between elastic and interfacial energy at the austenite-martensite interface implies that growth of a sufficiently small platelet always increases its energy (85). In short, there is a natural energy barrier to the growth of a nucleus.

Nuclei are stabilized by defects and are expected to have a variety of sizes. The energy barrier occurs at a particular size ℓ_c. If one treats ℓ_c as a constant characteristic of the material and defect structure, one arrives at a prediction of the width of the thermal hysteresis loop (85). This prediction turns out to be incredibly sensitive to a material constant λ_2, discussed in Section 3.2.1. In fact, according to this model, the predicted width of the hysteresis loop is zero when $\lambda_2 = 1$. As discussed below, $\lambda_2 = 1$ is a necessary and sufficient condition that austenite is perfectly compatible with a single variant of martensite. In that case, there is no need for the twinning (with or without branching) and the competition between bulk and interfacial energy is lost, as is the energy barrier. When λ_2 is close to 1, the calculation of hysteresis is extremely sensitive to λ_2. Predicted plots of hysteresis versus λ_2 based on this model are quantitatively similar to **Figure 11*b***. We discuss ways to modify λ_2 via compositional changes in Section 3.2.1.

In summary, there are two quite different thoughts about the origins of hysteresis in first-order phase transformations, but both relate to the austenite-martensite interface. One relates to defect formation arising in the stressed transition layer between phases as it propagates through the material, and the second relates to an energy barrier associated with the growth of a twinned platelet. Tuning λ_2 to 1 removes both the stressed layer and the energy barrier and is expected to be a broadly useful strategy to mitigate the losses caused by hysteresis in energy conversion devices.

3.1.2. Reversibility. Reversibility relates to changes in the material under repeated cycling. Functional fatigue is defined as the degradation of functional properties with cycling (88), whether

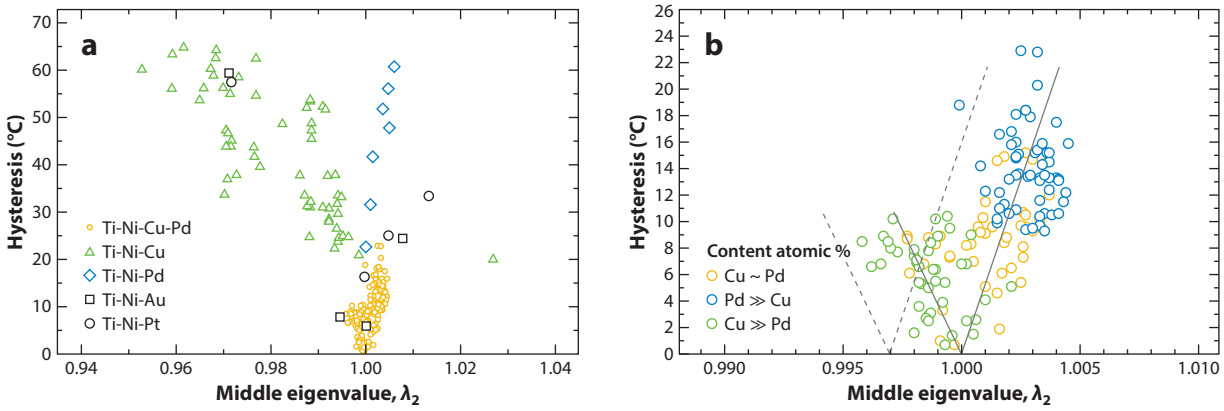

Figure 11

Measured thermal hysteresis versus λ_2 in alloys from a combinatorial library (*yellow circles* and *green triangles*) and from bulk alloys of Ti-Ni-(Cu, Pd, Pt, Au) (84, 85, 105). Each marker corresponds to a different alloy. Panel *b* is a close-up of panel *a* near $\lambda_2 = 1$. The dashed line in panel *b* indicates that a systematic correction of the data was made due to the presence of thin film stress (see 105). Note that the size of the hysteresis can be reduced to near zero by tuning the composition to satisfy $\lambda_2 = 1$. Panel *a* adapted from Reference 105 with permission from Elsevier; panel *b* adapted from Reference 83 with permission from the American Academy for the Advancement of Science.

thermal, mechanical, electrical, or magnetic. Structural fatigue concerns actual changes in the structure of the material, such as the creation of dislocations.

Recently, the reversibility of phase transformations has been studied under cyclic-stress-induced transformation (83, 86, 97). Stress is favored in such tests because it can be applied quickly such that multimillion-cycle tests become possible on bulk specimens at ordinary timescales. Besides conditions of compatibility, such as $\lambda_2 = 1$ and the cofactor conditions (described in Section 3.2.2), reversibility under the demanding conditions of stress-induced transformation is affected by grain size and the presence of precipitates (86). While stress is present due to electromagnetic forces, the energy conversion methods described here do not rely on the presence of applied stress, so one can expect that they are more forgiving with regard to reversibility.

3.2. Tuning Lattice Parameters for Low Hysteresis and High Reversibility

Conditions of compatibility between phases have a significant influence on hysteresis and reversibility, and they can be tuned by compositional changes.

3.2.1. The geometric constant λ_2. In simple phase transformations between Bravais lattices, there is a linear transformation represented by a 3×3 matrix $\mathbf{F}$ with a positive determinant that maps the high-symmetry parent lattice to the transformed lattice. In fact, there are infinitely many such matrices $\mathbf{F}$, because there are lattice-invariant deformations—that is, the infinitely many deformations that map a lattice to itself. Typically, we remove the degeneracy due to lattice-invariant deformations by choosing $\mathbf{F}$ to minimize the distortion (that is, to minimize, say, $|\mathbf{U} - \mathbf{I}|$, where $\mathbf{I}$ is the identity matrix and the notation $|\mathbf{A}|$ denotes the square root of the sum of the squares of the elements of the matrix $\mathbf{A}$). We can also rotate the transformed lattice in any way, so $\mathbf{QF}$ is also such a transformation, where $\mathbf{Q}$ is a 3×3 rotation matrix. Using the polar decomposition theorem, we choose $\mathbf{Q}$ so that $\mathbf{U} = \mathbf{QF}$ is positive-definite and symmetric. Then $\mathbf{U}$ is called the transformation stretch tensor (98). An algorithm for finding transformation stretch tensors for all transformations between Bravais lattices can be found at **http://www.structrans.org**.

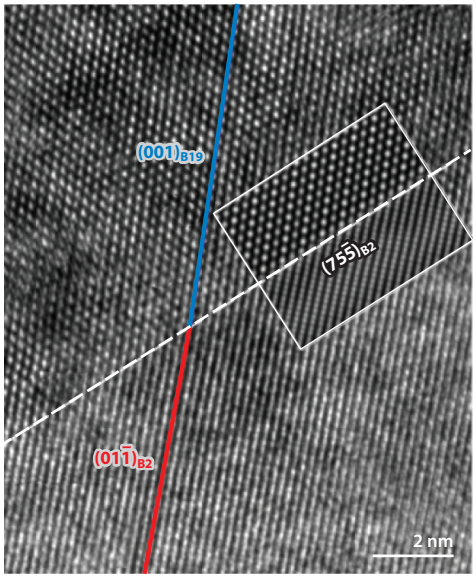

Figure 12

High-resolution micrograph of the interface between parent and transformed phases in $Ti_{50}Ni_{40}Pd_{10}$, which closely satisfies $\lambda_2 = 1$.

Rarely are crystalline phases representable as simple Bravais lattices, especially in the low-symmetry phases of magnetic martensites. However, in all cases, crystalline phases are representable as the union of a finite number of identical Bravais lattices. During a phase transformation between such phases, even in a complex case, each Bravais lattice undergoes the same linear transformation **U** (which we take as positive-definite and symmetric). The lattices can also undergo small displacements relative to one another; this is called shuffling. But even in the case of complex lattices, it is the transformation stretch tensor **U** that governs long-range stress fields and the fitting together of phases at an interface.

Being positive-definite and symmetric, the transformation stretch tensor **U** has three positive eigenvalues, which we order as $\lambda_1 \leq \lambda_2 \leq \lambda_3$. As noted in Section 2.2, due to the symmetry of the parent phase, there are variants of the transformed phase. Each variant has a transformation stretch tensor—for example, $\mathbf{U}_1, \ldots, \mathbf{U}_n$ for n variants. By symmetry, each of the tensors $\mathbf{U}_1, \ldots, \mathbf{U}_n$ has the same eigenvalue.

A basic theorem in phase transformations (69, 92, 97, 99) says that a necessary and sufficient condition for two phases to fit together perfectly at an interface is $\lambda_2 = 1$. Because λ_2 depends on the lattice parameters of the material, and the lattice parameters depend on the composition, there is the possibility to tune λ_2 to 1 via compositional changes. Recalling from the preceding section that a perfect, unstressed interface between phases would remove both sources of hysteresis, this becomes a powerful tool to reduce loss in energy conversion devices.

Numerous researchers have confirmed that the thermal hysteresis dramatically decreases as $\lambda_2 \to 1$ (84, 86, 97, 100–105). An example, taken from Reference 105, is shown in **Figure 11**, where each marker represents a different alloy. **Figure 12** shows a twinless austenite-martensite interface without an elastic transition layer in a $Ti_{50}Ni_{40}Pd_{10}$ alloy that closely satisfies $\lambda_2 = 1$ (102). These results (84, 105) highlight combinatorial synthesis methods as powerful tools for verifying or refuting hypotheses concerning the design of materials. This can be especially appreciated when it is realized that the Ni-Ti-X-Y system has been the most studied system for phase

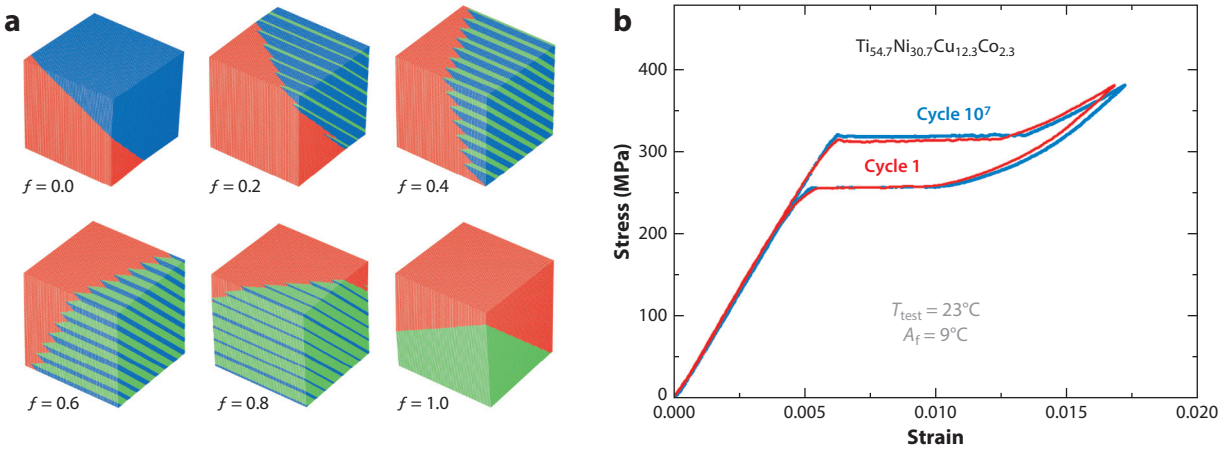

Figure 13

(*a*) Supercompatible interface exhibiting perfect fitting of the phases and zero elastic energy, despite a large distortion (87); *f* is the volume fraction of the blue-green variants. (*b*) Behavior of an alloy under stress-induced full transformation in tension, satisfying closely the cofactor conditions (83).

transformations in materials science since around 1980, yet despite the many alloy series that have been synthesized and characterized, this ability to tune hysteresis to near zero had not been recognized previously. Recent work shows that the relation between λ_2 and hysteresis applies also to oxide systems (106–108).

3.2.2. Cofactor conditions. The condition $\lambda_2 = 1$ is the first of three conditions called the cofactor conditions (86, 97, 100, 109). The cofactor conditions represent a degeneracy of the crystallographic theory of martensite that not only allows for a perfect unstressed interface between phases but also allows for complex arrangements of the phases with no transition layers—that is, zero elastic energy (86, 97, 109). The second and third of the cofactor conditions depend on the type of twin system, where the twin system types—type I, type II, and compound—are defined in, for example, References 69, 110, and 111. In particular, the second condition is $|\mathbf{U}^{-1}\hat{\mathbf{e}}| = 1$ for type I twins and $|\mathbf{U}\hat{\mathbf{e}}| = 1$ for type II twins, where $\mathbf{U}$ is the stretch tensor defined in Section 3.2.1 and $\hat{\mathbf{e}}$ is a unit vector aligned with the twofold axes associated with these twins. The third condition is a mild inequality that has to be checked but is usually satisfied.

When the cofactor conditions are satisfied, the material can form a great variety of zero-energy martensite microstructures with curved interfaces and variable twin phase fractions (87, 100). An example of a theoretical simulation of a material satisfying the cofactor conditions is shown in **Figure 13*a***. This should be contrasted with the classical case of **Figures 8** and **9**. A difference is that in the classical case (with or without branching), there are only four possible interfaces, given the twin system. **Figure 13** has a continuous variation of volume fraction; that is, it has infinitely many interfaces. All of these interfaces have zero elastic energy, in contrast to the interfacial layers in **Figures 8** and **9**, which have small elastic energy balanced by interfacial energy. **Figure 13*a*** is one of a plethora of zero-energy microstructures possible under the cofactor conditions, which include complex curved interfaces and nucleation mechanisms for austenite in martensite and martensite in austenite.

Currently, to our knowledge, there are two materials known that closely satisfy the cofactor conditions: $Zn_{45}Au_{30}Cu_{25}$ (100) and $Ti_{54.7}Ni_{30.7}Cu_{12.3}Co_{2.3}$ (83). They both exhibit an unprecedented response: The former has thermal hysteresis less than 1°C despite a 7% transformation

strain, and the latter exhibits the extraordinary reversibility shown in **Figure 13*b***. Both alloys behave with poor reversibility if the composition is tuned 2–3% away from the given composition. Two very recent studies show that the cofactor conditions are also effective for improving the reversibility of ceramic systems (108, 112).

The lowering of hysteresis and the unprecedented reversibility achieved under $\lambda_2 = 1$ and the other cofactor conditions indicate that completely removing stressed transition layers, not merely lowering their energy as indicated in **Figures 8–10**, is decisive. The term supercompatibility refers to this complete elimination of transition layers (86). Under conditions of supercompatibility, the balance between elastic energy and interfacial energy is disrupted, because there is no elastic energy to compete with the interfacial energy. A promising first principles high-throughput method for evaluating conditions of supercompatibility on ternary phase diagrams is presented in Reference 113.

While 10 million cycles (**Figure 13*b***) is far short of what is needed for energy conversion applications, it is reasonable to anticipate that crystals tuned to satisfy conditions of supercompatibility will have an acceptable level of reversibility under thermally induced transformations with no applied stress. Applying this procedure to engineer ferromagnetic or ferroelectric phase transformations for the purpose of highly reversible energy conversion is an open area.

3.3. Supercritical Behavior

A fertile area of research in the study of phase transformations is supercritical behavior. Supercritical transitions have potentially significant implications for ferroelectric and ferromagnetic energy conversion for two reasons: (*a*) Supercritical transitions may be highly reversible and thus may give rise to stable cyclic devices, and (*b*) extending thermodynamic cycles into the supercritical region is predicted to yield relatively large work outputs at high thermal efficiencies (24) (Section 5).

As in the case of supercritical fluids, the term supercritical here refers to a state above the critical point, or above the mixed-phase dome that can be seen in the temperature-entropy and polarization–electric field phase diagrams in **Figure 3*a*,*c***. Just as the liquid and gas phases are indistinguishable in a supercritical fluid, the parent and transformed phases are indistinguishable in a supercritical crystalline material. **Figure 3*a*,*c*** shows that the transition becomes smoother and more gradual. These transitions are sometimes called second-order-like first-order transformations in the literature. What is notable about supercritical behavior in phase transformations is the very-low-hysteresis (anhysteretic), often highly reversible macroscopic response. Supercritical behavior has recently been observed in $Ni_{50}Fe_{19}Co_4Ga_{27}$ (38, 40) and $Fe_{68.8}Pd_{31.2}$ (39, 114, 115) ferromagnetic shape memory alloys and may have been observed even earlier in other systems without being identified as supercritical or postcritical. For example, supercritical behavior can be seen in the accurate model (116) of the free energy of $BaTiO_3$. Its presence allows for interesting ways of increasing the efficiency of energy conversion devices (24).

4. FERROMAGNETIC ENERGY CONVERSION

4.1. Martensite and Magnetism

Energy conversion using first-order phase transformations between ferromagnetic and nonferromagnetic phases is discussed in References 21, 22, 54–57, and 76. Among materials used in demonstrations, the strongly ferromagnetic phase of La-Fe-Co-Si (57) is the low-temperature phase, while in $Ni_{45}Co_5Mn_{40}Sn_{10}$ (21, 76) or $Ni_{50.4}Co_{3.7}Mn_{32.8}In_{13.1}$ (55), it is the high-temperature phase (**Figure 14**). As noted in Section 2.1, we use $Ni_{45}Co_5Mn_{40}Sn_{10}$ (117) to explain the concepts.

Following the remarks in Section 3.2, it is worth noting that λ_2 is quite close to 1 in $Ni_{45}Co_5Mn_{40}Sn_{10}$ (117). An alloy that is quite similar in behavior to $Ni_{45}Co_5Mn_{40}Sn_{10}$, but

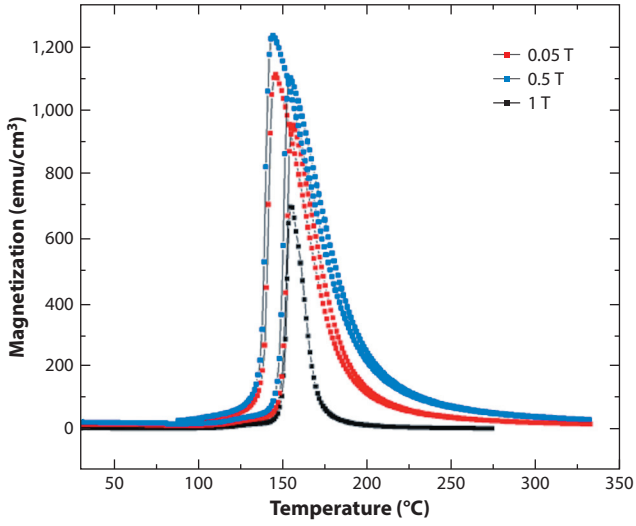

Figure 14

Magnetization versus temperature at several applied field strengths in $Ni_{45}Co_5Mn_{40}Sn_{10}$.

probably too expensive for energy conversion applications, is $Fe_{48}Rh_{52}$. $Fe_{48}Rh_{52}$ also has λ_2 close to 1. Both alloys could benefit from further tuning: The lowest achievable hysteresis in these systems is not known and would represent important proof-of-principle results in magnetic martensites.

Known values of λ_2 and measured hysteresis for Ni-Mn-X alloys (X = In, Sb, Sn) are given in Reference 22. Any of these could be considered starting points for alloy development to achieve strong magnetism and low hysteresis, as demonstrated by Devi et al. (118) in Ni-Mn-In. For this purpose, the Hume-Rothery parameter *e/a* provides an excellent parameterization of phase diagrams in these systems (119), vastly simplifying alloy development for both first-order phase transformations and strong magnetism.

4.2. Physics of Ferromagnetic Energy Conversion

The basic physics of energy conversion by a first-order ferromagnetic transformation in the simplest case is as follows (22). First, note that $Ni_{45}Co_5Mn_{40}Sn_{10}$ is quite magnetically soft: From **Figure 14**, applied fields as low as 0.05 T cause the material to achieve a large fraction of the saturation magnetization in the austenite phase. Thus, we place a permanent magnet below the device so that, when it transforms on heating, it becomes strongly magnetized (**Figure 15**). (Without this permanent magnet, the material would demagnetize itself.) Basic magnetostatics says that the magnetization distribution **M** of the phase-change material is partitioned between the magnetic field $\mathbf{H}_M$ and the magnetic induction $\mathbf{B}_M$ according to the fundamental dipolar relationship

$$\mathbf{B}_M = \mu_0(\mathbf{H}_M + \mathbf{M}). \quad 9.$$

How this partitioning occurs is critical to ferromagnetic energy conversion. It is the time-changing magnetic induction $d\mathbf{B}/dt$ that produces an electric current in the surrounding coil via Faraday's law:

$$\frac{d\mathbf{B}}{dt} = -\text{curl}\,\mathbf{E}. \quad 10.$$

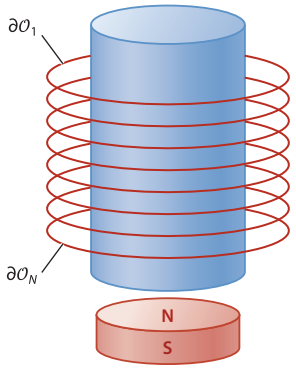

Figure 15

Schematic of the simplest energy conversion device using a ferromagnetic phase transformation. The phase-change material is blue. The dark red disk is a permanent magnet that is magnetized vertically.

Thus, we want the big $d\mathbf{M}/dt$ to translate into a big $d\mathbf{B}_M/dt$ via the time derivative of Equation 9. How this is done in practical terms is discussed in Section 4.3.

The partitioning represented by the dipole formula (Equation 9), together with the formulas of magnetostatics, div $\mathbf{B}_M = 0$ and curl $\mathbf{H}_M = 0$ (on all of space), implies that $\mathbf{B}_M$ and $\mathbf{H}_M$ are uniquely determined (as square integrable functions) by $\mathbf{M}$. That is, curl $\mathbf{H}_M = 0$ implies the existence of a magnetostatic potential $\mathbf{H}_M = -\nabla\psi_M$. Then div $\mathbf{B}_M = 0$ and Equation 9 imply $\Delta\psi_M = \text{div}\,\mathbf{M}$. Thus, given the magnetization $\mathbf{M}$, one solves $\Delta\psi_M = \text{div}\,\mathbf{M}$ on all of space to get ψ_M, from which $\mathbf{B}_M$ and $\mathbf{H}_M$ are determined. In summary, $\mathbf{B}_M$ and $\mathbf{H}_M$ are uniquely determined by the magnetization distribution $\mathbf{M}$, the laws of magnetostatics, and the dipolar relation $\mathbf{B}_M = \mu_0(\mathbf{H}_M + \mathbf{M})$.

Clearly, there are other field-producing sources in **Figure 15** besides $\mathbf{M}$. Because Maxwell's equations are linear, these additional fields add to $\mathbf{B}_M$ and $\mathbf{H}_M$. In particular, the time-changing total magnetic induction $\mathbf{B}$ induces a current $I(t)$ in the surrounding coil driven by the electric field in Equation 10. This current in turn produces a backfield, $\mathbf{H}_b$, given by the Biot-Savart law,

$$\mathbf{H}_b = \frac{1}{4\pi}\sum_{i=1}^{N}\oint_{\mathcal{O}_i}\frac{I\,d\ell\times\mathbf{r}}{|\mathbf{r}|^3}, \qquad 11.$$

where N is the number of turns $\mathcal{O}_1,\ldots,\mathcal{O}_N$ in the coil and $\mathbf{r}$ is a vector from a point on the coil to the point where $\mathbf{H}_b$ is being calculated. As explained in Reference 22, the backfield plays a critical role in energy conversion. The backfield decreases the total magnetic field applied to the material on heating and increases it on cooling. Accounting for the three sources, the total magnetic induction is then

$$\mathbf{B} = \mu_0(\mathbf{H}_0 + \mathbf{H}_b + \mathbf{H}_M + \mathbf{M}), \qquad 12.$$

where $\mathbf{H}_0$ is the time-independent field of the permanent magnet.

It is the total magnetic induction (Equation 12) that enters Faraday's law (Equation 10). The integrated form of Faraday's law, summed over the N turns to give the total voltage $V(t)$ across the coil, is

$$V = \sum_{i=1}^{N}\oint_{\mathcal{O}_i}\mathbf{E}\cdot d\ell = -\frac{d}{dt}\sum_{i=1}^{N}\oint_{\mathcal{O}_i}\mathbf{B}\cdot\mathbf{n}\,dA. \qquad 13.$$

Finally, this total voltage across the coil is related to the current $I(t)$ in the coil (see Equation 11) by Ohm's law:

$$I(t) = \frac{V(t)}{R + \rho\,\ell/a}, \tag{14.}$$

where R is the load resistance, ρ is the resistivity and ℓ the total length of the wire in the coil, and a is its cross-sectional area. Combining Equations 11–14, we arrive at the dynamical law for ferromagnetic energy conversion:

$$\begin{aligned} I(t)(R + \rho\,\ell/a) &= -\mu_0 \frac{\mathrm{d}}{\mathrm{d}t} \sum_{i=1}^{N} \oint_{\mathcal{O}_i} (\mathbf{H}_\mathrm{b} + \mathbf{M} + \mathbf{H}_\mathrm{M}) \cdot \mathbf{n}\,\mathrm{d}A \\ &= -\mu_0 \frac{\mathrm{d}}{\mathrm{d}t} \sum_{i=1}^{N} \oint_{\mathcal{O}_i} \left[\frac{1}{4\pi} \sum_{j=1}^{N} \oint_{\mathcal{O}_j} \frac{I(t)\,\mathrm{d}\ell \times \mathbf{r}}{|\mathbf{r}|^3} + \mathbf{M} + \mathbf{H}_\mathrm{M} \right] \cdot \mathbf{n}\,\mathrm{d}A \\ &= -\mu_0 \left[C \frac{\mathrm{d}I(t)}{\mathrm{d}t} + \frac{\mathrm{d}}{\mathrm{d}t} \sum_{i=1}^{N} \oint_{\mathcal{O}_i} (\mathbf{M} + \mathbf{H}_\mathrm{M}) \cdot \mathbf{n}\,\mathrm{d}A \right], \end{aligned} \tag{15.}$$

where C is a constant depending only on the coil design as

$$C = \frac{1}{4\pi} \sum_{i=1}^{N} \oint_{\mathcal{O}_i} \left(\sum_{j=1}^{N} \oint_{\mathcal{O}_j} \frac{\mathrm{d}\ell \times \mathbf{r}}{|\mathbf{r}|^3} \right) \cdot \mathbf{n}\,\mathrm{d}A. \tag{16.}$$

The last line of Equation 15 is an ordinary differential equation for the current, once the evolution of the magnetization is specified. The simplest assumption is to use a scalar model for magnetization and then to relate $\mathbf{H}_\mathrm{M}$ to $\mathbf{M}$ by using a demagnetization matrix. Experimental data can also be directly used to assign the volume average of $\mathbf{M}$ as a function of time (or temperature).

In addition to the evolution law for the current $I(t)$ in the coil, it is useful for ferromagnetic energy conversion to develop energy relations for the process, as in Reference 22. These are especially helpful in evaluating the role of other energies, such as elastic energies, that may be changing during a conversion cycle, as in Reference 55.

4.3. Role of Latent Heat, Backfield, Shape Effect, and Electromagnetic Forces

The rational design of effective energy conversion devices should account for the effect of the field on the transformation temperature, as discussed in Section 2.5, as well as the shape effect and electromagnetic forces.

In this respect, the backfield is critical. As shown in Section 4.2, the differing effect of the backfield on transformation temperature upon heating and cooling is directly responsible for the opening up of the mixed-phase region, which is the single most important factor for efficient energy conversion. More precisely, in the example of $Ni_{45}Co_5Mn_{40}Sn_{10}$, an axial applied field decreases transformation temperature according to the Clausius-Clapeyron equation, as expected due to the fact that the high-temperature phase is ferromagnetic. Then, the backfield decreases the total field on the specimen upon heating, and thus the transformation temperature is raised. Conversely, on cooling, it is lowered. Importantly, this splitting is affected by the latent heat as a key parameter in the Clausius-Clapeyron equation.

Another critical aspect of energy conversion revealed in Section 4.2 is the shape effect. As is familiar to experts in micromagnetics (see, e.g., 120), the partitioning of $\mathbf{M}$ into $\mathbf{B}_M$ and $\mathbf{H}_M$ is strongly affected by the shape of the domain Ω occupied by the magnetic material. But only the rate of change of $\mathbf{B}_M$ gives rise to the current in the coil. To maximize the variations of $\mathbf{B}_M$ during a cycle, a rodlike shape is desired, as in **Figure 15**, according to the shape effect. This restriction can be relaxed by the use of soft magnetic yokes that join rodlike phase-change materials, as in the topologies presented in Reference 57.

To our knowledge, there is little work on efficient heat transfer applicable to the methods of energy conversion reviewed here, yet it is a critical factor for power generation. It is clear that the shape effect particularly interacts with heat transfer issues. For example, the rodlike shape favored in the ferromagnetic case is not ideal for fast heat transfer. One could imagine overcoming this by having an array of thin rods, with a coil around all of them. But it is again known from micromagnetics that the electromagnetic interactions in a dense array are quite strong; that is, from the point of view of homogenization (collective behavior) and depending on overall aspect ratio, an array of rods can act effectively like a plate (121).

Magnetic forces can be quite strong. As shown in Reference 55, magnetic forces together with elastic forces can be used effectively to force the active material on and off a hot or cold surface at high frequency, thereby vastly improving power densities. Electromagnetic forces can also be used to introduce a self-starting function.

5. FERROELECTRIC ENERGY CONVERSION

Ferroelectric energy conversion using first-order phase transformations is a relatively unstudied area (23, 24), though there is a significant literature on pyroelectric energy conversion (42–47, 49, 50). Whereas one uses induction in the magnetic case, one uses capacitance in the ferroelectric case. A capacitive arrangement in the ferroelectric case opens up this area to the advanced methods of thin film technology, such as the use of modern methods of molecular beam epitaxial growth of oxides. This possibility could have significant benefits when the source is heat from computers or handheld electrical devices, because the energy conversion device can potentially be placed close to the chip and integrated with thin film technology. Major achievements of the past 10 years in the growth of extremely high-quality single-crystal films for microelectronic applications could have benefits for energy conversion.

A possible advantage of ferroelectric energy conversion over ferromagnetic energy conversion is that the ideal shape in the ferroelectric case is capacitive, that is, platelike. Thus, in ferroelectric energy conversion, the active material should be as thin as possible for high capacitance while avoiding dielectric breakdown. Following the remarks in Section 4.3, thinness is also desirable from the point of view of heat transfer.

5.1. First-Order Ferroelectric Phase Transformations

Ferroelectric materials owe their functional properties to first-order phase transformations exhibiting a large jump in polarization. Our prototype example, $BaTiO_3$, undergoes a first-order phase transformation from a paraelectric cubic phase to a strongly ferroelectric tetragonal phase upon cooling, followed by two additional transformations upon further cooling. The difference in electrical properties comes from the fact that the cubic phase is centrosymmetric and the tetragonal phase is noncentrosymmetric. When this transformation is induced under an electrical bias, it results in a >15 C/m^2 jump in polarization (116). The first-order nature of the phase transformation gives rise to a mixed-phase region that can potentially support high-efficiency thermodynamic

cycles (23). Ferroelectric materials such as $BaTiO_3$ that undergo phase transformations are also ferroelastic and piezoelectric and can thus be used to harvest vibrational energy. A hybrid technology that harvests and/or converts both waste heat and vibrational energy could be an interesting area of research (122–124).

As mentioned in Section 2, a critical role is played by the effect of the electric field on the transformation temperature in ferroelectrics. In an energy conversion device, this effect splits the transformation temperature so that the transformation occurs at a higher temperature upon heating and a lower temperature upon cooling, opening up the mixed-phase region. How this can be made to occur in a capacitive arrangement is discussed in Section 5.3. We note that, like in magnetic systems, the depolarization energy giving rise to the shape effect can be important in ferroelectric systems but is eliminated by free charges in the capacitive arrangement. In addition, the remarks in Section 2.4 also apply to ferroelectrics, so that typical internal twin boundaries are pole-free. For example, all variants of all three low-symmetry phases of $BaTiO_3$ are pole-free, since they give rise to type I, type II, or compound twins in all cases (69). While the optimization is different, a relevant literature for ferroelectric energy conversion is electrocaloric refrigeration (125) based on first-order phase transformations: Ferroelectric energy conversion cycles can be considered as electrocaloric cycles run backward.

5.2. Ferroelectric Materials for Energy Conversion

The desirable characteristics of a ferroelectric material for energy conversion at small temperature differences, using a first-order phase transformation, can be summarized as follows: large mixed-phase region, large jump in spontaneous polarization, suitable transformation temperature, low hysteresis, high degree of phase compatibility. The role of latent heat is subtle. In the absence of other factors, one would like a large latent heat to give a large electrical work output per cycle, according to the first law of thermodynamics. However, by the Clausius-Clapeyron equation, a large latent heat gives a small effect of the field on the transformation temperature, which restricts the size of the mixed-phase region and therefore the size of the cycle. Furthermore, a small latent heat may allow for higher-frequency operation, by speeding up the process of getting heat in and out of the device. [The latter is studied in first-order phase transformations in shape memory alloys (126, 127).] In the study of magnetocaloric devices, researchers have widely agreed that large latent heat is a main criterion to optimize, but the role of latent heat in the overall operation of energy conversion devices is, in our opinion, unclear at this time.

A ferroelectric with a large breakdown voltage may also be necessary, depending on the type of thermodynamic cycle used. In addition, the use of materials that are free of toxic and environmentally hazardous lead has become increasingly mandated over the past decade or so (128–132), particularly in Europe, which eliminates some potentially interesting choices. There are, however, many other possible first-order ferroelectric phase transformations to consider, and doping of ferroelectrics is widely possible. For example, as shown by Jaffe et al. (133, figure 5.28), $BaTiO_3$ can be doped with Co, Hf, Zn, Sn, Sr, and Ca, which modifies the transformation temperature and can also lower hysteresis by improving phase compatibility (106; see also 112). Many other possible lead-free starting points for ferroelectric materials development are listed in Reference 133.

The ferroelectric materials $BaTiO_3$ and Zr-doped $BaTiO_3$ were chosen in References 24 and 23, respectively. Generally, $BaTiO_3$ has several advantages: It is lead-free, has a low Curie temperature ($T_c = 120$–$130°C$) (134–136), has relatively low hysteresis (137, 138), and is already close to satisfying $\lambda_2 = 1$ at stoichiometry. For example, single-crystal $BaTiO_3$ lattice parameters published in References 139 and 140 result in λ_2 values of 0.992–0.998. This combination of properties makes this well-studied oxide a natural choice to demonstrate energy conversion at small temperature differences.

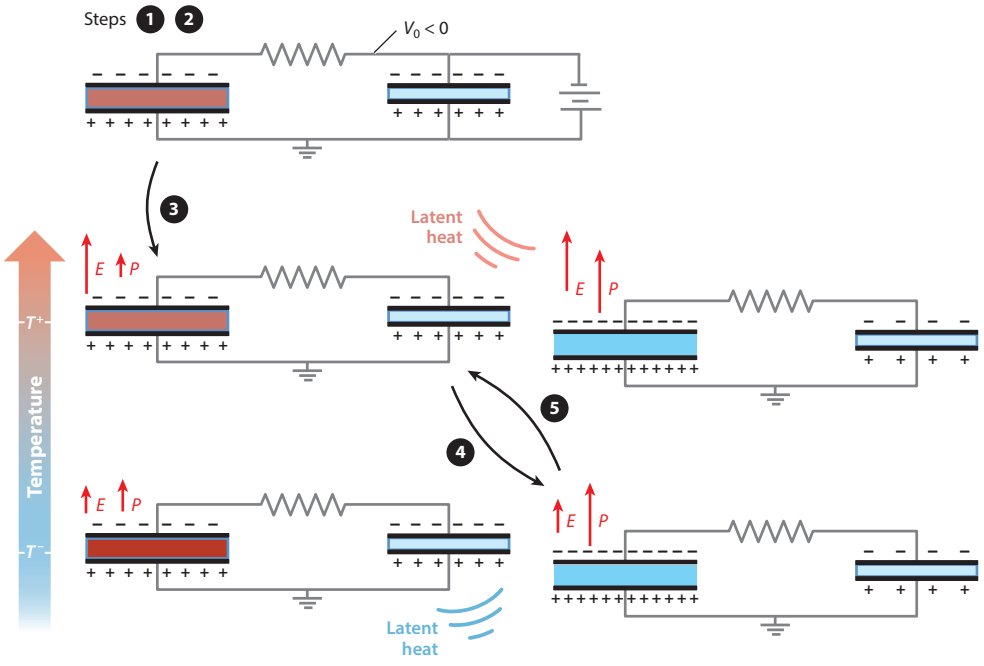

Figure 16

Steps ❶–❻ of the energy conversion procedure for ferroelectric energy conversion using a first-order phase transformation. The paraelectric phase is shown in dark red, and the ferroelectric phase is shown in blue.

5.3. Physics of Ferroelectric Energy Conversion

The physics of the ferroelectric energy conversion device is in some ways simpler than in the ferromagnetic case. The simplest possible arrangement is shown in **Figure 7**. The device consists of a two-capacitor arrangement with an active ferroelectric capacitor [in this case, a 0.5-mm-thick (100) $BaTiO_3$ single crystal (24)] connected in parallel to an ordinary capacitor. An electrical load between the two capacitors is represented by a resistor R. The ordinary capacitor has capacitance C_o. The energy conversion procedure is as follows (see **Figure 16**):

1. The ferroelectric capacitor is heated to T^+,
2. the circuit is charged to V_0 using an external battery,
3. the external battery is removed from the circuit,
4. the ferroelectric capacitor is cooled to T^-,
5. the ferroelectric capacitor is heated to T^+, and
6. steps 4 and 5 are repeated.

During step 2, some amount of total charge (represented by Q_{tot} in Equation 4) is introduced to the circuit; this charge distributes itself between the ferroelectric capacitor and the ordinary capacitor according to the two capacitances. Steps 1–3 can be thought of as priming the device. When the ferroelectric capacitor is cooled below the Curie temperature to T^-, the active material undergoes a phase transformation from the paraelectric phase to the ferroelectric phase, and the polarization jumps up. This increase in polarization attracts some of the charge from the ordinary capacitor, causing a current flow across the load. When the ferroelectric capacitor is heated back

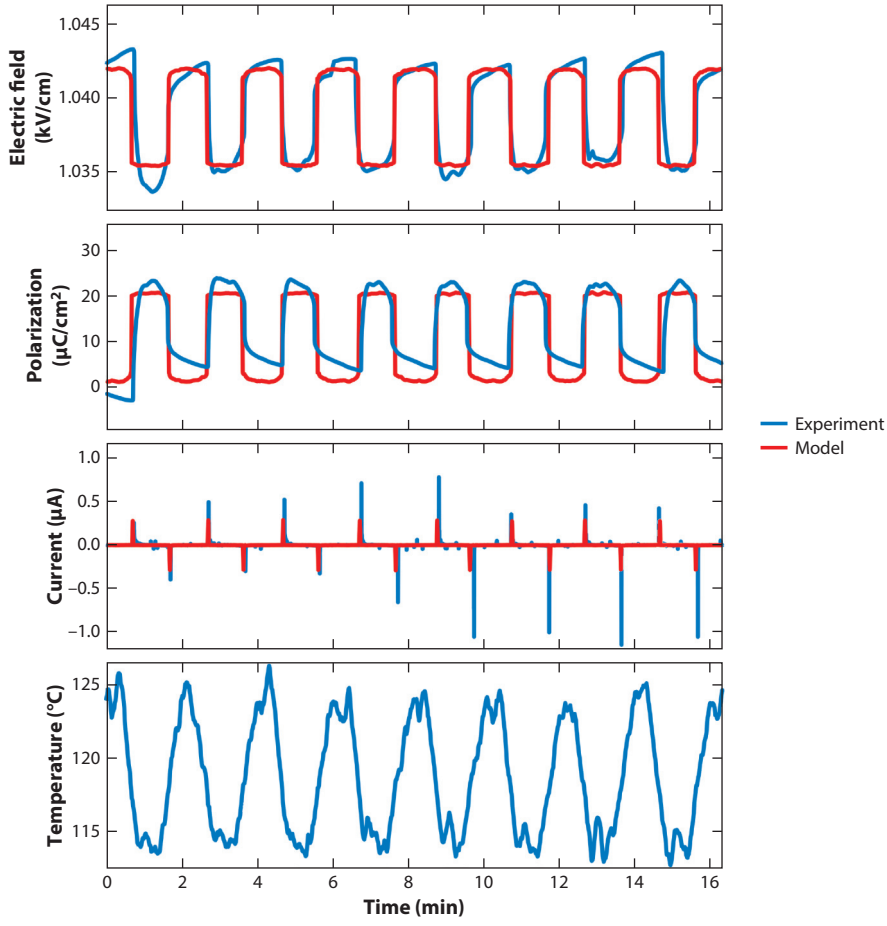

Figure 17

Theoretical versus experimental circuit response for ferroelectric energy conversion. The model is based on Equation 17, with the free energy from Wang et al. (116) (compare with **Figure 18**). The experimental conditions consist of heating and cooling a two-capacitor arrangement consisting of a ferroelectric and an ordinary capacitor (for more detail, see **Figure 16** and Reference 24). The input to the model is temperature versus time. Figure adapted from Reference 24.

above the Curie temperature to T^+, the polarization decreases, sending a current flow across the load back toward the ordinary capacitor.

A key point is that transformation on cooling from the paraelectric phase happens at a lower temperature than transformation on heating from the ferroelectric phase. This arises from the different electric fields in the capacitor during steps 4 and 5. That is, the Clausius-Clapeyron relation in Equation 7 predicts an increasing transformation temperature with electric field. During cooling from the paraelectric phase, there is a small electric field on the active capacitor giving a lower transformation temperature (see **Figures 17–19**). Conversely, when heating the ferroelectric phase, the electric field on the active capacitor is increased, and transformation occurs at a higher temperature.

The circuit response is easily characterized using Kirchhoff's laws, and the ferroelectric phase transformation can be modeled in the simplest case by a free energy $\varphi(P, T)$ of the type introduced

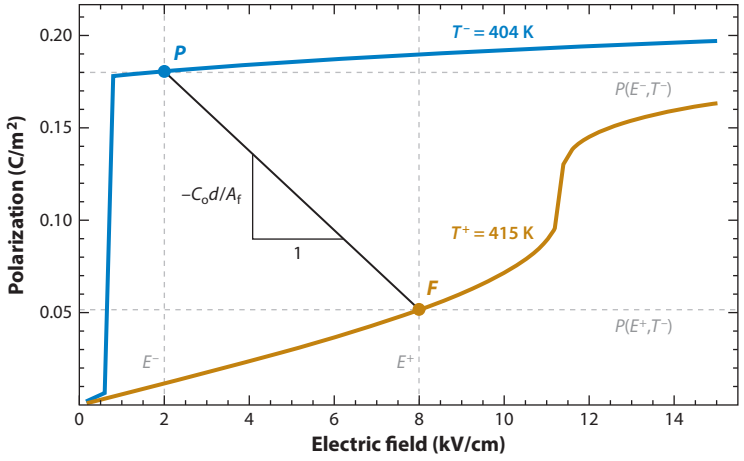

Figure 18

A method for optimizing the choice of the ordinary capacitor so as to achieve a large change of polarization. The slope of the straight line connecting the initial *P* state to the final *F* state is determined by the capacitance of the ordinary capacitor and the geometry of the active capacitor. Figure adapted from Reference 24.

in Section 2.5, based on the model in Reference 116. The result is a differential equation for the charge $Q_f(t)$ on the ferroelectric capacitor:

$$\dot{Q}_f(t) = \frac{Q_f(t) - Q_{tot}}{R C_o} - \left(\frac{d}{R}\right) \left.\frac{\partial \varphi[-Q_f(t)/A_f, T(t)]}{\partial P}\right|_{stable}. \qquad 17.$$

The subscript stable indicates that the energy minimization (Equation 4, or simply Equation 5, which is adequate in the present case) has been performed to locate stable branches of the free energy. A consequence of Equation 17 that is useful for designing the ordinary capacitor is illustrated in **Figure 18**; this result is obtained by integrating Equation 17 on an assigned temperature path $T(t)$ from T^- to T^+. The result says that the slope of the line connecting these two end states is $-C_o\, d_f/A_f$.

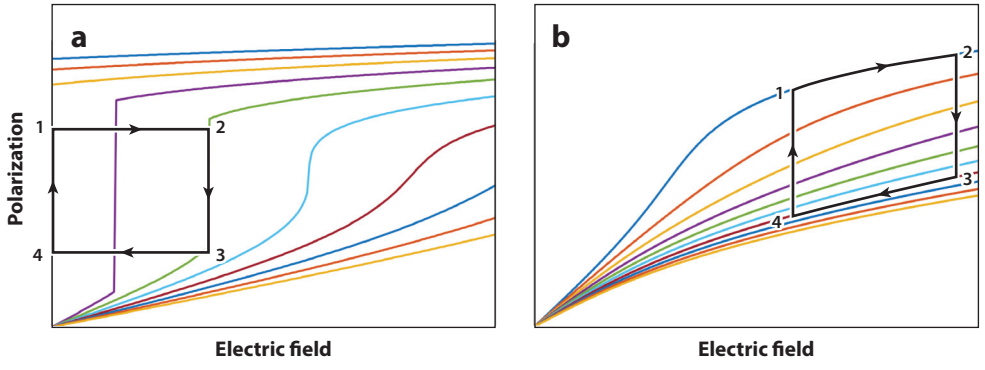

Figure 19

Schematic of (*a*) a Carnot cycle on a ferroelectric polarization–electric field diagram and (*b*) an Ericsson/Olsen cycle on a single-phase pyroelectric polarization–electric field diagram.

A comparison of theoretical and experimental responses for $BaTiO_3$ is shown in **Figure 17** with a 1 μF reference capacitor, a 5.1 kΩ resistor, $V_0 = 60$ V, and a measured temperature fluctuation between $T^+ = 124°C$ and $T^- = 114°C$. As the material transforms between the paraelectric phase at T^+ and the ferroelectric phase at T^-, the electric field and polarization can be seen jumping between two equilibrium states. The equilibrium state at T^+ is $P(E^+, T^+)$, E^+, and the equilibrium state at T^- is $P(E^-, T^-)$, E^-, where P is the polarization and E is the electric field. Each time the polarization jumps, the total charge is redistributed between the ferroelectric and ordinary capacitors, and current flows through the resistor. This current determines the power $[i(t)^2 R]$ being dissipated through the resistor.

If we assume that the free energy φ is first order in T, as in Reference 116, and the entropy S is as usual given by $S = -\frac{\partial \varphi}{\partial T}[P(E, T), T(E)]$, then a process with constant polarization is approximately isentropic. Thus, this relationship can give us an isentropic, constant polarization process for the construction of high-efficiency Rankine and Carnot cycles. This idea is implemented in Section 5.4 for a supercritical ferroelectric Carnot cycle.

5.4. Supercritical Carnot Cycles

Pyroelectric energy conversion researchers tend to favor Ericsson cycles, referred to as Olsen cycles in the pyroelectric literature after Randall B. Olsen (see 53). The idealized Ericsson cycle uses a cold gaseous working fluid such as air, consists of two isothermal and two isobaric processes, and has a theoretical efficiency equal to the Carnot efficiency. The pyroelectric version of the Ericsson cycle consists of two isothermal and two isoelectric field processes and is shown in **Figure 19*b***. When we look at **Figure 19*b***, it is clear why Ericsson cycles make sense for single-phase pyroelectric energy conversion: The temperature-entropy diagram of a single-phase pyroelectric material closely resembles that of a gaseous fluid, for which the Ericsson cycle was originally designed. In contrast, the temperature-entropy diagrams of ferroelectrics that undergo first-order phase transformations closely resemble those of first-order phase transformations in steam. For this reason, we draw inspiration from classical thermodynamic cycles that use first-order phase transformations in working fluids like steam, such as the idealized Rankine and Carnot cycles (see **Figure 19**).

Analogous to the ideal Carnot vapor cycle, the ideal ferroelectric Carnot cycle is composed of four reversible processes (**Figure 19**): adiabatic charging (1 to 2), isothermal depolarization (2 to 3), adiabatic discharging (3 to 4), and isothermal polarization (4 to 1).

Idealized Carnot cycles yield the maximum possible efficiency for a given temperature difference but have been considered impractical for energy conversion technologies, for example, with steam as the working fluid. However, in the ferroelectric case, a device that operates with near-perfect reversibility is conceivable through the use of highly reversible ferroelectric phase transformations, as discussed in Section 3. It is also possible to achieve effectively isentropic processes by using the relations discussed in Section 5.3. Drawing inspiration from Reference 141, one version of the ferroelectric Carnot cycle extends above the mixed-phase region (**Figure 20**) and is naturally termed a supercritical ferroelectric Carnot cycle. The practical implementation of the supercritical ferroelectric Carnot cycle uses the graphical relationship between equilibrium states shown in **Figure 18** (for details, see 24). Following this implementation, a temperature difference of 70°C is expected to produce an energy density of 1.15 J/cm^3 with a thermal efficiency of 15% according to theory. For comparison, the highest experimentally recorded values for energy density and efficiency reported for a pyroelectric heat-to-electricity converter using a ΔT of 70°C are 1.06 J/cm^3 and 3.6% (42). The latter, however, employed an attached battery, as discussed in Reference 23.

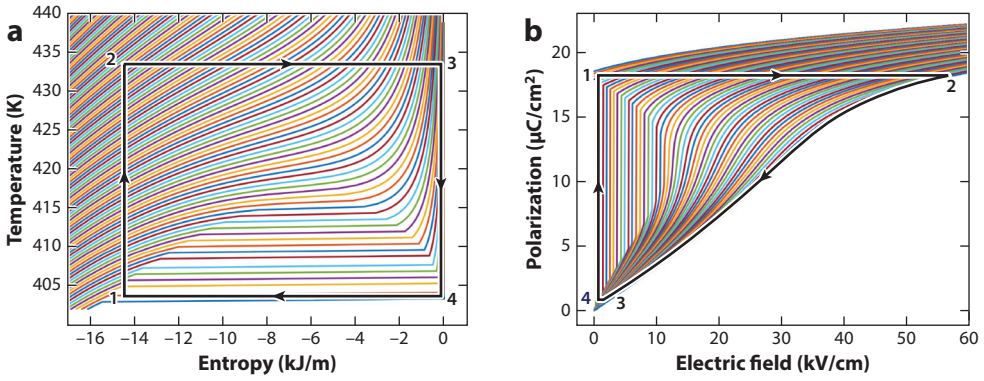

Figure 20

Simulated supercritical ferroelectric Carnot cycle shown for $BaTiO_3$ in (*a*) the temperature-entropy and (*b*) the polarization–electric field diagrams. Figure adapted from Reference 24.

In any capacitive system, leakage will eventually lead to losses. Losses in the energy conversion device itself can be compensated by periodic replenishing of the charge Q_{tot}, as effectively demonstrated in References 142 and 143. Similarly, our analysis of supercritical Carnot cycles (24) involves careful manipulation of the circuit, leading to temporary losses that are later recovered. Such compensation or manipulation provides valuable tools for optimization. However, overall measures of system efficiency used to compare different energy conversion devices must ensure that the device and surroundings (aside from the heat sources and the device that stores the energy produced) return exactly to their original states after each cycle, as emphasized in Reference 23.

6. OUTLOOK

In this review, we present a snapshot of the state of the art in the use of multiferroic first-order phase transformations for energy conversion. It is a rapidly developing subject whose basic physics is rather different from that of pyroelectric energy conversion or magnetic energy conversion near the second-order transition at the Curie temperature. It can be considered a promising method to contribute to the premier societal need of an energy conversion device for the small-temperature-difference regime.

We emphasize the key advantages of the first-order nature of the phase transformation. While the systems and physics are very different, these advantages are formally similar to the advantages of steam generation over single-phase gas generation, which underlie our present methods of energy generation. The key to exploiting the first-order phase transformations in multiferroic energy conversion is to open up a mixed-phase region in the temperature-entropy diagram by using the effect of electromagnetic fields on the transformation temperature.

The systems we present are of the simplest type. Major future improvements of these energy conversion methods are expected that are based on the design of cycles and circuits, co-designed with careful heat transfer analysis. Improved materials that have highly reversible transformations with large, abrupt changes of magnetization or polarization will be critical. Better first principles methods that can cope with finite temperature, nonstoichiometry, and strong correlations will be needed to locate interesting phase boundaries. Clearly, they need to be much more closely integrated with continuum theory to enable the design of materials with low hysteresis and high reversibility.

For the experimentally realized devices reviewed here, there remain barriers to reduction to practice. In the magnetic case, the known materials are either expensive or quite brittle, so the development of new lower-cost robust alloys with large changes of magnetization at the transformation is needed. In addition, the conflict between the shape effect and efficient heat transfer discussed in Section 4.3 presents a problem for magnetic devices. In the ferroelectric case, the devices presented have significant potential; the main barrier to reduction to practice is the lack of robust ferroelectric phase transformations that have a variety of transformation temperatures in the small-temperature-difference regime. Leakage also remains somewhat of a problem for the existing devices.

The development of thin film energy conversion devices could profoundly change the landscape of ferroelectric energy conversion. Such films combine the desirable features of thinness for high capacitance (in the ferroelectric phase) with fast heat transfer. High-quality single-crystal films may also mitigate leakage. In general, big first-order phase transformations in films are a neglected subject. We are only now beginning to understand the profound effect of constraint on the transformation temperature. In addition, the whole subject of hysteresis and reversibility, presented for bulk materials in Section 3, will likely need to be rethought for phase transformations in films.

DISCLOSURE STATEMENT

The authors are not aware of any affiliations, memberships, funding, or financial holdings that might be perceived as affecting the objectivity of this review.

ACKNOWLEDGMENTS

A.N.B. was supported by the University of Minnesota President's Postdoctoral Fellowship Program. B.J., W.N., and R.D.J. were supported by the Renewable Development Fund of the Institute on the Environment at the University of Minnesota, and W.N. received support from the Norwegian Centennial Chair. The preparation of this review also benefited from the support of the Multidisciplinary University Research Initiative program (FA9550-18-1-0095, FA9550-16-1-0566), the National Science Foundation (DMREF-1629026), the Office of Naval Research (N00014-18-1-2766), and a Vannevar Bush Faculty Fellowship. We acknowledge valuable discussions on first-order phase transformations and energy conversion with Sherry Xian Chen, Ole Martin Løvvik, Eckhard Quandt, and Yintao Song.

LITERATURE CITED

1. Giampietro M, Mayumi K. 2009. *The Biofuel Delusion: The Fallacy of Large-Scale Agro-Biofuels Production*. Abingdon, UK: Earthscan
2. Searchinger T, Heimlich R, Houghton RA, Dong F, Elobeid A, et al. 2008. Use of US croplands for biofuels increases greenhouse gases through emissions from land-use change. *Science* 319:1238–40
3. York R. 2012. Do alternative energy sources displace fossil fuels? *Nat. Clim. Change* 2:441–43
4. Intergov. Panel Clim. Change. 2013. *Climate Change 2013: The Physical Science Basis. Contribution of Working Group I to the Fifth Assessment Report of the Intergovernmental Panel on Climate Change*, ed. TF Stocker, D Qin, GK Plattner, M Tignor, SK Allen, et al. Cambridge, UK: Cambridge Univ. Press
5. Anderson K. 2015. Duality in climate science. *Nat. Geosci.* 8:898–900
6. Int. Energy Agency. 2008. *World Energy Outlook 2008*. Paris: Int. Energy Agency
7. Int. Energy Agency. 2018. *World Energy Outlook 2018*. Paris: Int. Energy Agency

8. Lawrence Livermore Natl. Lab. 2017. *Estimated U.S. energy consumption in 2016*. Publ. LLNL-MI-410527, Lawrence Livermore Natl. Lab., Livermore, CA
9. Miró L, Brückner S, Cabeza LF. 2015. Mapping and discussing industrial waste heat (IWH) potentials for different countries. *Renew. Sustain. Energy Rev.* 51:847–55
10. Johnson I, Choate WT, Davidson A. 2008. *Waste heat recovery: technology and opportunities in the U.S. industry*. Tech. Rep., US Dep. Energy, Washington, DC
11. Koomey JG. 2011. *Growth in data center electricity use 2005 to 2010*. Rep., Anal. Press, El Dorado Hills, CA
12. Corcoran P, Andrae A. 2013. *Emerging trends in electricity consumption for consumer ICT*. Tech. Rep., Natl. Univ. Irel., Galway
13. Dayarathna M, Wen Y, Fan R. 2016. Data center energy consumption modeling: a survey. *IEEE Commun. Surv. Tutor.* 18:732–94
14. Shehabi A, Smith SJ, Horner N, Azevedo I, Brown R, et al. 2016. *United States data center energy usage report*. Rep. LBNL-1005775, Lawrence Berkeley Natl. Lab., Berkeley, CA
15. Papapetrou M, Kosmadakis G, Cipollina A, Commare UL, Micale G. 2018. Industrial waste heat: estimation of the technically available resource in the EU per industrial sector, temperature level and country. *Appl. Therm. Eng.* 138:207–16
16. Ball P. 2012. Computer engineering: feeling the heat. *Nature* 492:174–76
17. Wikipedia. 2019. List of solar thermal power stations. *Wikipedia*. **https://en.wikipedia.org/wiki/List_of_solar_thermal_power_stations**
18. Vallis GK. 2017. *Atmospheric and Oceanic Fluid Dynamics: Fundamentals and Large-Scale Circulation*. Cambridge, UK: Cambridge Univ. Press. 2nd ed.
19. Bussières N, Granger RJ. 2007. Estimation of water temperature of large lakes in cold climate regions during the period of strong coupling between water and air temperature fluctuations. *J. Atmos. Ocean. Technol.* 24:285–96
20. Zhao D, Aili A, Zhai Y, Xu S, Tan G, et al. 2019. Radiative sky cooling: fundamental principles, materials, and applications. *Appl. Phys. Rev.* 6:021306
21. Srivastava V, Song Y, Bhatti K, James RD. 2011. The direct conversion of heat to electricity using multiferroic alloys. *Adv. Energy Mater.* 1:97–104
22. Song Y, Leighton C, James RD. 2016. Thermodynamics and energy conversion in Heusler alloys. In *Heusler Alloys: Properties, Growth, Applications*, ed. C Felser, A Hirohata, pp. 269–91. Cham, Switz.: Springer
23. Zhang C, Song Y, Wegner M, Quandt E, Chen X, et al. 2019. Power-source-free analysis of pyroelectric energy conversion. *Phys. Rev. Appl.* 12:014063
24. Bucsek A, Nunn W, Jalan B, James RD. 2019. Direct conversion of heat to electricity using first-order phase transformations in ferroelectrics. *Phys. Rev. Appl.* 12:034043
25. Tritt TM. 2011. Thermoelectric phenomena, materials, and applications. *Annu. Rev. Mater. Res.* 41:433–48
26. Bell LE. 2008. Cooling, heating, generating power, and recovering waste heat with thermoelectric systems. *Science* 321:1457–61
27. Satterthwaite CB, Ure RW. 1957. Electrical and thermal properties of Bi_2Te_3. *Phys. Rev.* 108:1164–70
28. Lee SW, Yang Y, Lee HW, Ghasemi H, Kraemer DM, et al. 2014. An electrochemical system for efficiently harvesting low-grade heat energy. *Nat. Commun.* 5:3942
29. Straub AP, Yip NY, Lin S, Lee J, Elimelech M. 2016. Harvesting low-grade heat energy using thermo-osmotic vapour transport through nanoporous membranes. *Nat. Energy* 1:16090
30. Hiscock T, Warner M, Palffy-Muhoray P. 2011. Solar to electrical conversion via liquid crystal elastomers. *J. Appl. Phys.* 109:104506
31. Schiller EH. 2002. *Heat engine driven by shape memory alloys: prototyping and design*. Master's Thesis, Va. Polytech. Inst. State Univ., Blacksburg
32. Bhattacharya K, James RD. 2005. The material is the machine. *Science* 307:53–54
33. Lang SB. 2005. Pyroelectricity: from ancient curiosity to modern imaging tool. *Phys. Today* 58:31–36

34. Giguere A, Foldeaki M, Gopal BR, Chahine R, Bose TK, et al. 1999. Direct measurement of the "giant" adiabatic temperature change in $Gd_5Si_2Ge_2$. *Phys. Rev. Lett.* 83:2262–65
35. Cross LE. 1987. Relaxor ferroelectrics. *Ferroelectrics* 76:241–67
36. Bhatti KP, El-Khatib S, Srivastava V, James RD, Leighton C. 2012. Small-angle neutron scattering study of magnetic ordering and inhomogeneity across the martensitic phase transformation in $Ni_{50-x}Co_xMn_{40}Sn_{10}$ alloys. *Phys. Rev. B* 85:134450
37. Monroe JA, Raymond JE, Xu X, Nagasako M, Kainuma R, et al. 2015. Multiple ferroic glasses via ordering. *Acta Mater.* 101:107–15
38. Kosogor A, L'vov VA, Chernenko VA, Villa E, Barandiaran JM, et al. 2014. Hysteretic and anhysteretic tensile stress–strain behavior of Ni–Fe(Co)–Ga single crystal: experiment and theory. *Acta Mater.* 66:79–85
39. Kakeshita T, Xiao F, Fukuda T. 2016. Large elastic strain and elastocaloric effect caused by lattice softening in an iron-palladium alloy. *Philos. Trans. R. Soc. A* 374:20150312
40. Chernenko VA, L'vov VA, Kabra S, Aseguinolaza IR, Kohl M, et al. 2018. Large anhysteretic deformation of shape memory alloys at postcritical temperatures and stresses. *Phys. Status Solidi B* 255:1700273
41. Yang Y, Wang L, Dong C, Xu G, Morosuk T, Tsatsaronis G. 2013. Comprehensive exergy-based evaluation and parametric study of a coal-fired ultra-supercritical power plant. *Appl. Energy* 112:1087–99
42. Pandya S, Wilbur J, Kim J, Gao R, Dasgupta A, et al. 2018. Pyroelectric energy conversion with large energy and power density in relaxor ferroelectric thin films. *Nat. Mater.* 17:432–38
43. Lee FY, Jo HR, Lynch CS, Pilon L. 2013. Pyroelectric energy conversion using PLZT ceramics and the ferroelectric–ergodic relaxor phase transition. *Smart Mater. Struct.* 22:025038
44. Sebald G, Pruvost S, Guyomar D. 2007. Energy harvesting based on Ericsson pyroelectric cycles in a relaxor ferroelectric ceramic. *Smart Mater. Struct.* 17:015012
45. Khodayari A, Pruvost S, Sebald G, Guyomar D, Mohammadi S. 2009. Nonlinear pyroelectric energy harvesting from relaxor single crystals. *IEEE Trans. Ultrason. Ferroelectr. Freq. Control* 56:693–99
46. Clingman WH, Moore RG. 1961. Application of ferroelectricity to energy conversion processes. *J. Appl. Phys.* 32:675–81
47. Childress JD. 1962. Application of a ferroelectric material in an energy conversion device. *J. Appl. Phys.* 33:1793–98
48. Olsen RB, Evans D. 1983. Pyroelectric energy conversion: hysteresis loss and temperature sensitivity of a ferroelectric material. *J. Appl. Phys.* 54:5941–44
49. Navid A, Vanderpool D, Bah A, Pilon L. 2010. Towards optimization of a pyroelectric energy converter for harvesting waste heat. *Int. J. Heat Mass Transf.* 53:4060–70
50. Navid A, Pilon L. 2011. Pyroelectric energy harvesting using Olsen cycles in purified and porous poly(vinylidene fluoride-trifluoroethylene) [P(VDF-TrFE)] thin films. *Smart Mater. Struct.* 20:025012
51. Olsen RB, Briscoe JM, Bruno DA, Butler WF. 1981. A pyroelectric energy converter which employs regeneration. *Ferroelectrics* 38:975–78
52. Olsen RB, Brown DD. 1982. High efficiency direct conversion of heat to electrical energy-related pyroelectric measurements. *Ferroelectrics* 40:17–27
53. Olsen RB, Bruno DA, Briscoe JM. 1985. Pyroelectric conversion cycles. *J. Appl. Phys.* 58:4709–16
54. Christiaanse T, Brück E. 2014. Proof-of-concept static thermomagnetic generator experimental device. *Metall. Mater. Trans. E* 1:36–40
55. Gueltig M, Ossmer H, Ohtsuka M, Miki H, Tsuchiya K, et al. 2014. High frequency thermal energy harvesting using magnetic shape memory films. *Adv. Energy Mater.* 4:1400751
56. Gueltig M, Wendler F, Ossmer H, Ohtsuka M, Miki H, et al. 2017. High-performance thermomagnetic generators based on Heusler alloy films. *Adv. Energy Mater.* 7:1601879
57. Waske A, Dzekan D, Sellschopp K, Berger D, Stork A, et al. 2019. Energy harvesting near room temperature using a thermomagnetic generator with a pretzel-like magnetic flux topology. *Nat. Energy* 4:68–74
58. Tesla N. 1890. *Pyromagneto-electric generator*. US Patent 428,057
59. Guzmán-Verri GG, Littlewood PB, Varma CM. 2013. Paraelectric and ferroelectric states in a model for relaxor ferroelectrics. *Phys. Rev. B* 88:134106
60. Hill NA. 2000. Why are there so few magnetic ferroelectrics? *J. Phys. Chem. B* 104:6694–709

61. Eerenstein W, Mathur N, Scott JF. 2006. Multiferroic and magnetoelectric materials. *Nature* 442:759–65
62. Spaldin NA. 2011. *Magnetic Materials: Fundamentals and Applications*. Cambridge, UK: Cambridge Univ. Press. 2nd ed.
63. Bain EC. 1924. The nature of martensite. *Trans. AIME* 70:25–35
64. Bowles JS, Mackenzie JK. 1954. The crystallography of martensitic transformations I. *Acta Metall.* 2:129–37
65. Bowles JS, Mackenzie JK. 1954. The crystallography of martensitic transformations II. *Acta Metall.* 2:138–47
66. Wayman CM. 1964. *Introduction to the Crystallography of Martensitic Transformations*. New York: Macmillan
67. Khachaturyan AG. 1983. *Theory of Structural Transformations in Solids*. Mineola, NY: Dover
68. Duerig TW. 1990. *Engineering Aspects of Shape Memory Alloys*. London: Butterworth-Heinemann
69. Bhattacharya K. 2003. *Microstructure of Martensite: Why It Forms and How It Gives Rise to the Shape Memory Effect*. Oxford, UK: Oxford Univ. Press
70. Bhattacharya K, Conti S, Zanzotto G, Zimmer J. 2004. Crystal symmetry and the reversibility of martensitic transformations. *Nature* 428:55–59
71. Dawber M, Rabe KM, Scott JF. 2005. Physics of thin-film ferroelectric oxides. *Rev. Mod. Phys.* 77:1083–130
72. James RD, Kinderlehrer D. 1993. Theory of magnetostriction with applications to $Tb_xDy_{1-x}Fe_2$. *Philos. Mag. B* 68:237–74
73. Shu YC, Bhattacharya K. 2001. Domain patterns and macroscopic behaviour of ferroelectric materials. *Philos. Mag. B* 81:2021–54
74. Post A, Knight C, Kisi E. 2013. Thermomagnetic energy harvesting with first order phase change materials. *J. Appl. Phys.* 114:033915
75. Hohenberg P, Kohn W. 1964. Inhomogeneous electron gas. *Phys. Rev.* 136:B864–71
76. Song Y, Bhatti KP, Srivastava V, Leighton C, James RD. 2013. Thermodynamics of energy conversion via first order phase transformation in low hysteresis magnetic materials. *Energy Environ. Sci.* 6:1315–27
77. James RD, Hane KF. 2000. Martensitic transformations and shape-memory materials. *Acta Mater.* 48:197–222
78. Brahlek M, Gupta AS, Lapano J, Roth J, Zhang HT, et al. 2018. Frontiers in the growth of complex oxide thin films: past, present, and future of hybrid MBE. *Adv. Funct. Mater.* 28:1702772
79. Jalan B, Moetakef P, Stemmer S. 2009. Molecular beam epitaxy of $SrTiO_3$ with a growth window. *Appl. Phys. Lett.* 95:032906
80. Prakash A, Xu P, Faghaninia A, Shukla S, Ager JW III, et al. 2017. Wide bandgap $BaSnO_3$ films with room temperature conductivity exceeding 10^4 S cm^{-1}. *Nat. Commun.* 8:15167
81. Prakash A, Jalan B. 2019. Wide bandgap perovskite oxides with high room-temperature electron mobility. *Adv. Mater. Interfaces* 6:1900479
82. Li YL, Hu SY, Liu ZK, Chen LQ. 2002. Effect of electrical boundary conditions on ferroelectric domain structures in thin films. *Appl. Phys. Lett.* 81:427–29
83. Chluba C, Ge W, de Miranda RL, Strobel J, Kienle L, et al. 2015. Ultralow-fatigue shape memory alloy films. *Science* 348:1004–7
84. Cui J, Chu YS, Famodu OO, Furuya Y, Hattrick-Simpers J, et al. 2006. Combinatorial search of thermoelastic shape-memory alloys with extremely small hysteresis width. *Nat. Mater.* 5:286–90
85. Zhang Z, James RD, Müller S. 2009. Energy barriers and hysteresis in martensitic phase transformations. *Acta Mater.* 57:4332–52
86. Gu H, Bumke L, Chluba C, Quandt E, James RD. 2018. Phase engineering and supercompatibility of shape memory alloys. *Mater. Today* 21:265–77
87. Chen X, Song Y, Dabade V, James RD. 2013. Study of the cofactor conditions: conditions of supercompatibility between phases. *J. Mech. Phys. Solids* 61:2566–87
88. Eggeler G, Hornbogen E, Yawny A, Heckmann A, Wagner M. 2004. Structural and functional fatigue of NiTi shape memory alloys. *Mater. Sci. Eng. A* 378:24–33

89. Norfleet DM, Sarosi PM, Manchiraju S, Wagner MFX, Uchic MD, et al. 2009. Transformation-induced plasticity during pseudoelastic deformation in Ni-Ti microcrystals. *Acta Mater.* 57:3549–61
90. Wechsler MS, Lieberman DS, Read TA. 1953. On the theory of the formation of martensite. *Trans. AIME* 197:1503–15
91. Lieberman DS, Wechsler MS, Read TA. 1955. Cubic to orthorhombic diffusionless phase change—experimental and theoretical studies of AuCd. *J. Appl. Phys.* 26:473–84
92. Ball JM, James RD. 1987. Fine phase mixtures as minimizers of energy. *Arch. Ration. Mech. Anal.* 100:13–52
93. Bronstein E, Faran E, Shilo D. 2019. Analysis of austenite-martensite phase boundary and twinned microstructure in shape memory alloys: the role of twinning disconnections. *Acta Mater.* 164:520–29
94. Straka L, Drahokoupil J, Veřtát P, Kopeček J, Zelenỳ M, et al. 2017. Orthorhombic intermediate phase originating from {110} nanotwinning in $Ni_{50.0}Mn_{28.7}Ga_{21.3}$ modulated martensite. *Acta Mater.* 132:335–44
95. Kohn RV, Müller S. 1992. Branching of twins near an austenite–twinned-martensite interface. *Philos. Mag. A* 66:697–715
96. Seiner H, Plucinsky P, Dabade V, Benešová B, James RD. 2019. Branching of twins in shape memory alloys revisited. arXiv:1910.05235 [cond-mat.mtrl-sci]
97. Chen X, Srivastava V, Dabade V, James RD. 2013. Study of the cofactor conditions: conditions of supercompatibility between phases. *J. Mech. Phys. Solids* 61:2566–87
98. Chen X, Song Y, Tamura N, James RD. 2016. Determination of the stretch tensor for structural transformations. *J. Mech. Phys. Solids* 93:34–43
99. James RD, Hane KF. 2000. Martensitic transformations and shape-memory materials. *Acta Mater.* 48:197–222
100. Song Y, Chen X, Dabade V, Shield TW, James RD. 2013. Enhanced reversibility and unusual microstructure of a phase-transforming material. *Nature* 502:85–88
101. Delville R, Schryvers D, Zhang Z, James RD. 2009. Transmission electron microscopy investigation of microstructures in low-hysteresis alloys with special lattice parameters. *Scr. Mater.* 60:293–96
102. Delville R, Kasinathan S, Zhang Z, Humbeeck JV, James RD, Schryvers D. 2010. Transmission electron microscopy study of phase compatibility in low hysteresis shape memory alloys. *Philos. Mag.* 90:177–95
103. Shi H, Delville R, Srivastava V, James RD, Schryvers D. 2014. Microstructural dependence on middle eigenvalue in Ti–Ni–Au. *J. Alloys Compd.* 582:703–7
104. Bucsek AN, Hudish GA, Bigelow GS, Noebe RD, Stebner AP. 2016. Composition, compatibility, and the functional performances of ternary NiTiX high-temperature shape memory alloys. *Shape Mem. Superelast.* 2:62–79
105. Zarnetta R, Takahashi R, Young ML, Savan A, Furuya Y, et al. 2010. Identification of quaternary shape memory alloys with near-zero thermal hysteresis and unprecedented functional stability. *Adv. Funct. Mater.* 20:1917–23
106. Wegner M, Gu H, James RD, Quandt E. 2020. Correlation between phase compatibility and efficient energy conversion in Zr-doped barium titanate. *Sci. Rep.* 10:3496
107. Jetter J, Gu H, Zhang H, Wuttig M, Chen X, et al. 2019. Tuning crystallographic compatibility to enhance shape memory in ceramics. *Phys. Rev. Mater.* 3:093603
108. Liang YG, Lee S, Yu HS, Zhang HR, Bendersky LA, et al. 2019. Tuning the hysteresis of a metal-insulator transition via lattice compatibility. arXiv:1905.01398 [cond-mat.mtrl-sci]
109. James RD, Zhang Z. 2005. A way to search for multiferroic materials with unlikely combinations of physical properties. In *Magnetism and Structure in Functional Materials*, ed. A Planes, L Manõsa, A Saxena, pp. 159–75. Berlin: Springer-Verlag
110. Bilby BA, Crocker AG. 1965. The theory of the crystallography of deformation twinning. *Proc. R. Soc. A* 288:240–55
111. Hane KF, Shield TW. 1999. Microstructure in the cubic to monoclinic transition in titanium-nickel shape memory alloys. *Acta Mater.* 47:2603–17
112. Pang EL, McCandler CA, Schuh CA. 2019. Reduced cracking in polycrystalline ZrO_2-CeO_2 shape-memory ceramics by meeting the cofactor conditions. *Acta Mater.* 177:230–39

113. Pike NA, Matt A, Løvvik OM. 2019. Determining the optimal phase-change material via high-throughput calculations. *MRS Adv.* 4:2679–87
114. Xiao F, Fukuda T, Kakeshita T. 2015. Critical point of martensitic transformation under stress in an Fe-31.2Pd (at.%) shape memory alloy. *Philos. Mag.* 95:1390–98
115. Seiner H, Stoklasová P, Sedlák P, Ševčík M, Janovská M, et al. 2016. Evolution of soft-phonon modes in Fe-Pd shape memory alloy under large elastic-like strains. *Acta Mater.* 105:182–88
116. Wang YL, Tagantsev AK, Damjanovic D, Setter N, Yarmarkin VK, et al. 2007. Landau thermodynamic potential for $BaTiO_3$. *J. Appl. Phys.* 101:104115
117. Srivastava V, Chen X, James RD. 2010. Hysteresis and unusual magnetic properties in the singular Heusler alloy $Ni_{45}Co_5Mn_{40}Sn_{10}$. *Appl. Phys. Lett.* 97:014101
118. Devi P, Mejía CS, Zavareh MG, Dubey KK, Kushwaha P, et al. 2019. Improved magnetostructural and magnetocaloric reversibility in magnetic Ni-Mn-In shape-memory Heusler alloy by optimizing the geometric compatibility condition. *Phys. Rev. Mater.* 3:062401
119. Bhatti KP, Srivastava V, Phelan DP, El-Khatib S, James RD, Leighton C. 2016. Magnetic phase competition in off-stoichiometric martensitic Heusler alloys: the $NiCo_xMn_{25+y}Sn_{25-y}$ system. In *Heusler Alloys: Properties, Growth, Applications*, ed. C Felser, A Hirohata, pp. 193–216. Cham, Switz.: Springer
120. Brown WF. 1963. *Micromagnetics*. New York: Interscience
121. Krishnan SN. 2012. *Asymptotic models in magnetostriction with application to design of sensors*. PhD Diss., Univ. Minn., Minneapolis
122. Erturun U, Waxman R, Green C, Richeson ML, Mossi K. 2010. Energy scavenging combining piezoelectric and pyroelectric effects. In *Proceedings of the ASME 2010 Conference on Smart Materials, Adaptive Structures and Intelligent Systems*, Vol. 2, pp. 53–59. New York: Am. Soc. Mech. Eng.
123. Wang ZL. 2013. Triboelectric nanogenerators as new energy technology for self-powered systems and as active mechanical and chemical sensors. *ACS Nano* 7:9533–57
124. Bowen CR, Taylor J, LeBoulbar E, Zabek D, Chauhan A, Vaish R. 2014. Pyroelectric materials and devices for energy harvesting applications. *Energy Environ. Sci.* 7:3836–56
125. Mischenko AS, Zhang Q, Scott JF, Whatmore RW, Mathur ND. 2006. Giant electrocaloric effect in thin-film $PbZr_{0.95}Ti_{0.05}O_3$. *Science* 311:1270–71
126. Leo PH, Shield TW, Bruno OP. 1993. Transient heat transfer effects on the pseudoelastic behavior of shape-memory wires. *Acta Metall. Mater.* 41:2477–85
127. Shaw JA, Kyriakides S. 1995. Thermomechanical aspects of NiTi. *J. Mech. Phys. Solids* 43:1243–81
128. Saito Y, Takao H, Tani T, Nonoyama T, Takatori K, et al. 2004. Lead-free piezoceramics. *Nature* 432:84–87
129. Takenaka T, Nagata H. 2005. Current status and prospects of lead-free piezoelectric ceramics. *J. Eur. Ceram. Soc.* 25:2693–700
130. Ringgaard E, Wurlitzer T. 2005. Lead-free piezoceramics based on alkali niobates. *J. Eur. Ceram. Soc.* 25:2701–6
131. Priya S, Nahm S. 2011. *Lead-Free Piezoelectrics*. New York: Springer
132. Coondoo I, Panwar N, Kholkin A. 2013. Lead-free piezoelectrics: current status and perspectives. *J. Adv. Dielectr.* 3:1330002
133. Jaffe B, Cook WR Jr., Jaffe H. 1971. *Piezoelectric Ceramics*. London: Academic
134. Rhodes RG. 1951. Barium titanate twinning at low temperatures. *Acta Crystallogr.* 4:105–10
135. von Hippel A, Breckenridge RG, Chesley FG, Tisza L. 1946. High dielectric constant ceramics. *Ind. Eng. Chem.* 38:1097–109
136. Buhrer CF. 1962. Some properties of bismuth perovskites. *J. Chem. Phys.* 36:798–803
137. Curecheriu L, Balmus SB, Buscaglia MT, Buscaglia V, Ianculescu A, Mitoseriu L. 1998. Grain size-dependent properties of dense nanocrystalline barium titanate ceramics. *J. Am. Ceram. Soc.* 95:3912–21
138. Kanata T, Yoshikawa T, Kubota K. 1987. Grain-size effects on dielectric phase transition of $BaTiO_3$ ceramics. *Solid State Commun.* 62:765–67
139. Wang JJ, Meng FY, Ma XQ, Xu MX, Chen LQ. 2010. Lattice, elastic, polarization, and electrostrictive properties of $BaTiO_3$ from first-principles. *J. Appl. Phys.* 108:034107

140. Kwei GH, Lawson AC, Billinge SJL, Cheong SW. 1993. Structures of the ferroelectric phases of barium titanate. *J. Phys. Chem.* 97:2368–77
141. Iverson BD, Conboy TM, Pasch JJ, Kruizenga AM. 2013. Supercritical CO_2 Brayton cycles for solar-thermal energy. *Appl. Energy* 111:957–70
142. McKay T, O'Brien B, Calius E, Anderson I. 2012. Self-priming dielectric elastomer generator design. In *Proceedings of SPIE*, Vol. 8340: *Electroactive Polymer Actuators and Devices (EAPAD) 2012*, p. 83401Y. Bellingham, WA: SPIE
143. McKay T, O'Brien B, Calius E, Anderson I. 2010. Self-priming dielectric elastomer generators. *Smart Mater. Struct.* 19:055025
144. Heczko O, Straka L, Seiner H. 2013. Different microstructures of mobile twin boundaries in 10 M modulated Ni–Mn–Ga martensite. *Acta Mater.* 61:622–31
145. Straka L, Heczko O, Seiner H, Lanska N, Drahokoupil J, et al. 2011. Highly mobile twinned interface in 10 M modulated Ni–Mn–Ga martensite: analysis beyond the tetragonal approximation of lattice. *Acta Mater.* 59:7450–63
146. Ganor Y, Dumitrica T, Feng F, James RD. 2016. Zig-zag twins and helical phase transformations. *Philos. Trans. R. Soc. Lond. A* 374:20150208
147. Knüpfer H, Kohn RV, Otto F. 2013. Nucleation barriers for the cubic-to-tetragonal phase transformation. *Commun. Pure Appl. Math.* 66:867–904